https://doi.org/10.5194/acp-2020-846
Preprint. Discussion started: 22 October 2020

Atmospheric Chemistry and Physics Discussions

An Estimate of Global, Regional and Seasonal Cirrus Cloud Radiative Effects Contributed by Homogeneous Ice Nucleation

David L. Mitchell[1], John Mejia[1], Anne Garnier[2], Yuta Tomii[1], Martina Krämer[3,4] and Farnaz Hosseinpour[1]

[1]Desert Research Institute, Reno, 89512-1095, USA
[2]Science Systems and Applications, Inc., Hampton, Virginia, USA
[3]Institute for Energy and Climate Research (IEK-7), Research Center Jülich, Jülich, Germany
[4]Institute for Atmospheric Physics (IPA), Johannes Gutenberg University, Mainz, Germany
Correspondence to: David Mitchell (david.mitchell@dri.edu)

Abstract. There are two fundamental mechanisms through which cirrus clouds form; homo- and heterogeneous ice nucleation (henceforth hom and het). The relative contribution of each mechanism to ice crystal production often determines the microphysical and radiative properties of a cirrus cloud. This study attempts to estimate the radiative contribution of hom relative to het by constraining the cloud microphysics in a climate model to conform with satellite retrievals of cirrus cloud effective diameter D_e, where the sampled cirrus cloud base had a temperature T < 235 K (-38 °C). The CALIPSO (*Cloud-Aerosol Lidar and Infrared Pathfinder Satellite Observation)* satellite retrievals for cirrus clouds are compared against an updated in situ cirrus cloud property climatology to evaluate similarities and differences. In this climate modeling study, we ask how the cloud radiative effect (CRE) based on retrieved cirrus cloud properties compares with the CRE predicted by a model configuration representing cirrus clouds formed only through het and also with the CRE predicted by the standard configuration of the model. To answer this question, we constrained version 2 of the Morrison-Gettelman cloud microphysics scheme (MG2), which is used in several climate models, using effective diameter (D_e) retrievals from the CALIPSO satellite. A new subroutine within the MG2 scheme provides retrieved D_e as a function of temperature (T), latitude, season and land fraction, while ice particle mass and area relationships are used to relate D_e to the ice particle size distribution (PSD) slope and to produce new relationships for the number- and mass-weighted ice fall speeds. These and other modifications rendered the MG2 microphysics consistent with the D_e constraint. Using 40-year simulations of the Whole Atmosphere Community Climate Model version 6 (WACCM6), the CRE outside the tropics from the D_e-constrained WACCM6 was greater than standard WACCM6 by 1.63 W m^{-2} in the Northern Hemisphere (NH) and 2.59 W m^{-2} in the Southern Hemisphere (SH). Using the version of WACCM6 designed to represent cirrus clouds formed only by het (instead of using standard WACCM6), this difference was 2.37 W m^{-2} in the NH and 2.55 W m^{-2} in the SH. These differences are larger when only non-summer months are considered.

https://doi.org/10.5194/acp-2020-846
Preprint. Discussion started: 22 October 2020

Atmospheric Chemistry and Physics Discussions

1 Introduction

Cirrus clouds contain only ice particles (i.e. no liquid cloud droplets), a condition guaranteed when cloud temperatures (T) are less than ~ -38° C. Their ice crystals can form by either of two mechanisms; homogeneous or heterogeneous ice nucleation (henceforth hom and het). The former requires no ice nucleating particles (INP) and can proceed through the freezing of haze and cloud solution droplets when T ≤ 235 K (-38° C) and the relative humidity with respect to ice (RHi) exceeds some threshold where RHi > ~ 145% (Koop, 2000). This results in relatively high concentrations of ice particles (N), where in situ measurements of N are typically > ~ 200 L^{-1} ($liter^{-1}$) whereas het generally produces N < ~ 200 L^{-1} (Barahona and Nenes, 2009; Jensen et al., 2012a, b; Cziczo et al., 2013). Under very cold and unique conditions of weak and relatively short-lived updrafts (e.g. low-amplitude gravity waves), N resulting from hom may be < 100 L^{-1} (Sprichtinger and Krämer, 2013; Krämer et al., 2016), and under atypical conditions (such as high concentrations of mineral dust), N resulting from het can exceed 200 L^{-1}. In cirrus clouds, het may occur at any RHi > 100%, and in the context of a cloud parcel moving in an updraft, ice is first produced through het, and subsequently through hom if the het-produced ice crystals do not prevent the RHi from reaching the threshold RHi needed for hom to occur (e.g. Haag et al., 2003). Overall, cirrus clouds formed primarily through hom will likely have substantially higher N and smaller effective diameters (D_e) relative to cirrus formed primarily through het. For a given ice water content (IWC) or ice mass mixing ratio (q_i) and temperature range, these two types of cirrus clouds will therefore display considerably different radiative properties, making it critical to properly attribute hom and het in climate modeling.

Current climate models capable of predicting hom and het in cirrus clouds assume that ice nucleation occurs in the presence of pre-existing ice crystals (i.e. the pre-existing ice assumption; Shi et al., 2015). This strongly favors het over hom since the pre-existing crystals may exhibit considerable ice surface area (relative to new ice crystals) and prevail in the competition for water vapor, preventing the RHi from reaching the RHi threshold for hom. This assumption is universally applied under all conditions.

However, it is possible that hom plays a larger role in cirrus clouds than currently predicted in climate models. For example, the satellite remote sensing study by Zhao et al. (2018) demonstrated hom had a strong impact on cirrus cloud microphysics under relatively clean (relatively low aerosol optical depth) conditions. Another satellite remote sensing study by Sourdeval et al. (2018) shows that N in cirrus clouds (T < 235 K) outside the tropics is relatively high during the winter season, with relatively low N for T > 235 K. This same result (highest N during winter) was observed in the cirrus cloud remote sensing studies of Mitchell et al. (2016; 2018), who suggested that hom was more active during winter due to a reduction of convective mixing of ice nucleating particles (INP) from the surface to cirrus cloud levels. Anvil cirrus, most common during summer, contain advected pre-existing ice that may also enhance het. These studies also found N outside the tropics (± 30° latitude) was higher over mountainous terrain,

https://doi.org/10.5194/acp-2020-846
Preprint. Discussion started: 22 October 2020


Atmospheric Chemistry and Physics Discussions

attributing this to mountain-induced wave clouds having relatively strong and sustained updrafts (and thus greater cooling rates producing high supersaturations) conducive for hom. This was also observed in the satellite remote sensing study of Gryspeerdt et al. (2018) that explained the higher N over mountainous terrain in a similar way. In both studies N was highest near cloud top, which appeared to directly affect N at lower levels.

In addition, Mitchell et al. (2016; 2018) found that N was relatively high at high latitudes. This was explained by the relatively pristine conditions associated with relatively low concentrations of INPs, especially over the Southern Ocean (Vergara-Temprado et al., 2018; McCluskey, 2018). That is, when N produced by het is relatively low, the ice surface area produced is often inadequate to prevent the RHi from climbing and reaching the hom threshold in a cirrus cloud updraft, resulting in higher N produced by hom. Similar results over the Southern Ocean are shown in Figure 1 of Gryspeerdt et al. (2018).

Motivated by these findings, an experiment was designed to investigate the radiative impact of hom (relative to het) on spatial and temporal (i.e. seasonal) scales. The experiment combined CALIPSO (*Cloud-Aerosol Lidar and Infrared Pathfinder Satellite Observation)* satellite retrievals of effective diameter (D_e) with climate modeling, where D_e was used to constrain the cloud microphysics treatment in the climate model. The climate model was constrained in two ways; one based on global D_e retrievals while the other was based on D_e characteristic of het conditions. Differences between these two constrained versions are expected to reveal the impact of hom.

Specifically, D_e is used to constrain version 2 of the Morrison-Gettelman cloud microphysics scheme (MG2; Gettelman and Morrison, 2015; Gettelman et al., 2015), used in the Community Atmosphere Model version 6 (CAM6), the Whole Atmosphere Community Climate Model version 6 (WACCM6), and version 2 of the Community Earth System Model (CESM2). For this study, WACCM6 is used to capture potential changes to the stratosphere. The methodology in Section 2 describes how D_e is used to determine the ice particle size distribution (PSD) slope and the number- and mass-weighted ice fall speeds, as well as other aspects. The experimental design is described in Section 3, followed by a comparison in Section 4 between the D_e retrievals and a recently developed climatology of cirrus cloud ice particle properties. Section 5 contains the results and discussions thereof, and conclusions are given in Section 6.

2 Methodology

A CALIPSO satellite remote sensing method designed for cirrus clouds uses co-located measurements from the Infrared Imaging Radiometer (IIR) and the CALIOP (Cloud and Aerosol Lidar with Orthogonal Polarization) lidar aboard CALIPSO to retrieve N by exploiting the sensitivity of the effective absorption optical depth ratio, β_{eff}, to small ice crystals, where this ratio is based on the 10.6 and 12.05 μm IIR channels. Also retrieved are D_e, ice water content (IWC), ice water path (IWP) and cloud visible optical depth (OD) for single-layer cirrus clouds having $0.3 \leq$

https://doi.org/10.5194/acp-2020-846
Preprint. Discussion started: 22 October 2020

Atmospheric Chemistry and Physics Discussions

OD ≤ 3.0, where cloud base having a temperature ≤ 235 K is always detected. This retrieval is described in Mitchell et al. (2016; 2018) where two years are evaluated to analyze the dependence of cirrus cloud N and D_e on altitude, temperature, latitude, season and surface type (i.e. ocean vs. land, or land-fraction). This two-year data set is used in this study to constrain D_e in the WACCM6 that uses the MG2 scheme. That is, six 30° latitude zones, four seasons and ocean vs. land designations were used to produce 48 D_e-T relationships defined in look-up tables (LUTs). These D_e LUTs are contained within a subroutine that is called by the MG2 scheme to produce a cirrus cloud D_e for a given T, latitude, season and land-fraction. From this D_e are calculated the cirrus PSD slope λ and corresponding number- and mass-weighted ice fall speeds V_N and V_m. The CALIPSO retrieval's sensitivity to N renders median D_e as small as 11 μm, resulting in very narrow PSD under some conditions where V_N and V_m are not predicted well by the standard MG2 scheme. For this reason and others we developed new expressions for V_N and V_m.

2.1 Calculating the cirrus PSD slope parameter from D_e

To constrain the MG2 scheme with D_e retrievals requires modifying the MG2 physics to ensure that the physics is compatible and consistent with this constraint. This means that λ must be derived from the retrieved D_e, beginning with the PSD growth stage at ice nucleation and sustaining this λ thereafter. This was done by calculating λ from D_e by inverting equation (14) in Erfani and Mitchell (2016; henceforth EM2016):

$$\lambda = \left[\frac{2\,\rho_i\,\gamma\,\Gamma(\delta+\nu+1)\,D_e}{3\,\alpha\,\Gamma(\beta+\nu+1)} \right]^{[1/(\delta-\beta)]} \quad (1)$$

where Γ denotes the gamma function, ρ_i = bulk density of ice (0.917 g cm-3), ν = PSD dispersion parameter = 0 in the MG2 scheme, and α, β, γ and δ are the ice particle mass (m) and projected area (A) coefficients in their respective power laws:

$$m = \alpha\, D^{\beta}, \quad (2)$$

$$A = \gamma\, D^{\delta}, \quad (3)$$

where D is the ice particle maximum dimension. Unfortunately, these coefficients, α, β, γ and δ, are weakly dependent on D, and Eq. (1) is only accurate over the D-range associated with λ and D_e, especially at relatively small D. To account for this non-linearity, m and A are calculated as described in EM2016:

$$\ln m = a_0 + a_1 \ln D + a_2 (\ln D)^2, \quad (4)$$

$$\ln A = b_0 + b_1 \ln D + b_2 (\ln D)^2, \quad (5)$$

https://doi.org/10.5194/acp-2020-846
Preprint. Discussion started: 22 October 2020

Atmospheric Chemistry and Physics Discussions

where a_0, a_1, b_0 and b_1 are constants. Note that ln denotes natural log and m, A and D are in g, cm^2 and cm. See Tables 1 and 2 in EM2016 for the coefficients to apply, using the temperature interval for -40 to -55 °C and synoptic cirrus clouds. Note that using curves for other temperature intervals and/or anvil cirrus makes little difference in these relationships since they are similar. Note that the PSD mean ice particle size, D_{mean}, is related to λ as $D_{mean} = (\nu + 1)/\lambda$ for an analytical gamma size distribution given as:

$$N(D) = N_0 D^{\nu} \exp(-\lambda D), \quad (6)$$

where N_0, ν and λ are constants. As described in EM2016, an iterative solution employing Eqns. (4), (5) and (1) yields an accurate relationship between D_{mean} and D_e, and thus λ and D_e. This relationship is shown by the orange circles in Fig. 1, and a curve-fit to this solution is given by this equation (black curve in Fig. 1):

$$\ln(D_{mean}) = -8.727 (-0.1962 \ln(D_e) + 1.0)^{1/2} + 7.680, \quad (7)$$

where D_{mean} and D_e are in micron units. Although the EM2016 ice particle mass and projected area relationships (i.e. Eqns. (4) and (5)) are technically valid down to D = 20 μm, these relationships were extrapolated down to D_{mean} = 1 μm to produce Eq. (7). In doing so, they were constrained to not exceed the value of an ice sphere (ρ_{ice} = 0.917 g cm^{-3}) having the same D. This affected D_{mean} < 27 μm for projected area and D_{mean} < 10 μm for mass. These relationships are based on synoptic cirrus clouds for -55°C < T < -40°C, given in Table 2 of EM2016. Similar m-D and A-D relationships are given in EM2016 for other temperature intervals as well as for anvil cirrus clouds, but there was generally not much variation among these relationships. Therefore, the m-D/A-D relationships used here are considered representative for all cirrus clouds. These relationships were utilized in a manner similar to the way they were used to produce Fig. 13 in EM2016. Specifically,

$$\beta = a_1 + 2 a_2 \ln D_m , \quad (8)$$

$$\alpha = \exp[a_0 + a_1 \ln D_m + a_2 (\ln D_m)^2] / D_m^{\beta} , \quad (9)$$

where D_m is the median mass dimension, given for a gamma PSD as

$$D_m = (\beta + \nu + 0.67)/\lambda. \quad (10)$$

The equations giving δ and γ are analogous to Eqns. (8) and (9), but use different constants that are given in Table 2 of EM2016 for synoptic cirrus clouds, -55°C < T < -40°C, and are based on D_A, the median area dimension, given in EM2016 as

$$D_A = (\delta + \nu + 0.67)/\lambda. \quad (11)$$

https://doi.org/10.5194/acp-2020-846
Preprint. Discussion started: 22 October 2020


Atmospheric Chemistry and Physics Discussions

To generate the data in Fig. 1, D_{mean} was incremented, and new values for α, β, γ and δ were calculated as above for each D_{mean} for use in Eq. (1) to solve for D_e. Moreover, D_e is commonly defined as

$$D_e = (3/2)\ IWC/(\rho_i\ A_{PSD})\ , \tag{12}$$

where IWC and A_{PSD} are the PSD ice water content and projected area, respectively, and ρ_i is the bulk density of ice (Mitchell, 2002). Due to its dependence on IWC, D_m is used to calculate α and β in Eqns. (8) and (9), and due to its dependence on A_{PSD}, D_A is used to calculate γ and δ in this iterative solution for D_e. This is the most accurate way we know of for calculating the relationship between D_e and D_{mean}, especially at small values of D_e that correspond to the smaller retrieved values of D_e. If $D_{mean} > 3$ mm (3000 μm), then $D_e = 166$ μm since Eq. (7) asymptotes to this value. Since (7) may not be valid for $D_{mean} > 3000$ μm, for cirrus, $D_{mean} \leq 3000$ μm in this modified MG2 scheme.

2.2 Calculation of ice particle fall speeds

Two PSD slope values are used in the MG2 scheme, one for cloud ice (λ_i) and one for snow (λ_s). Since we are forcing predicted cirrus clouds in MG2 to conform with CALIPSO retrievals of D_e, both λ_i and λ_s have the same value corresponding to the retrieved D_e. The number- and mass-weighted ice fall speeds, V_N and V_m, can be expressed as a function of D_{mean} and D_e, respectively, over the entire range of observed D_{mean} and D_e in cirrus clouds as shown in Mishra et al. (2014). Thus, if V_N and V_m are formulated in this way, it is not necessary to have separate expressions for V_N and V_m for cloud ice and snow, which is the current practice in the MG2 scheme. Therefore, in this modified treatment of cirrus clouds, we have a single expression for V_N as a function of D_{mean}, and a single expression for V_m as a function of D_e.

We use the same definition of V_N and V_m as found in the MG2 scheme:

$$V_N = (\rho_o/\rho)^{0.35}\ a\ \Gamma(b + \nu + 1) / \Gamma(\nu + 1)\ \lambda^b\ , \tag{13}$$

$$V_m = (\rho_o/\rho)^{0.54}\ a\ \Gamma(b + \beta + \nu + 1)/ \Gamma(\beta + \nu + 1)\ \lambda^b\ , \tag{14}$$

where *a* and *b* refer to the prefactor and exponent of an empirical fall speed power law:

$$V = a\ D^b\ , \tag{15}$$

ρ is air density and ρ_o is ρ at a reference pressure and temperature of 850 hPa and 273 K. For number weighted cloud ice, the MG2 scheme uses 0.35 as the power for the ratio ρ_o/ρ, but otherwise uses 0.54 based on Heymsfield et al. (2007). Since this fall speed treatment is only for cirrus clouds, an exponent of 0.35 appears most appropriate for V_N. The difference with this new approach is that *a*, *b* and β are constantly updated as a function of ice particle size. This process for β is described above. In Mitchell (1996), *a* and *b* are defined theoretically as

https://doi.org/10.5194/acp-2020-846
Preprint. Discussion started: 22 October 2020

Atmospheric Chemistry and Physics Discussions

$$V = c\,\mu\,\left[\frac{2\,\alpha\,g}{\rho\,\mu^2\,\gamma}\right]^{d}\,D^{d(\beta+2-\delta)-1} \quad (16)$$

where *a* in Eq. (15) is defined by the terms preceding D and *b* is defined by the power term for D. The terms *c* and *d* are constants describing the particle flow regime in Mitchell (1996), but are variables in this treatment that depend on ice particle size and mass as described in Mitchell and Heymsfield (2005). They relate the Best number X with the Reynolds number Re:

$$Re = c\,X^{d}\,. \quad (17)$$

When calculating V_n, the median number concentration dimension D_N is used to obtain *c* and *d* from the Mitchell-Heymsfield (2005) scheme, as well as α, β, γ and δ as described in Sect. 2.1 (analogous to D_m and D_A), where $D_N = (\nu + 0.67)/\lambda$. When calculating V_m, the median mass dimension D_m from Eq. (10) is used to obtain *c* and *d* in Eq. (16), as well as for α, β, γ and δ used in Eq. (16). In other words, D in Eq. (16) takes on the value of either D_N or D_m. The variables μ and ρ are kinematic viscosity and air density, and g is the gravitation constant, where $\mu = \eta/\rho$ and η is the dynamic viscosity, estimated as:

$$\eta = 2.48 \times 10^{-6}\,(T^{0.754}), \quad (18)$$

with T in degrees Kelvin and η is in g cm^{-1} s^{-1}. Air density is given as

$$\rho = p\,/\,(R_a\,T), \quad (19)$$

where p = pressure in dynes cm^{-2} (equals p in hPa × 1000), $R_a = 2.867\times10^6$ erg g^{-1} K^{-1} is the gas constant for dry air, T is in K and ρ is in g cm^{-3} (multiply by 10^3 for kg m^{-3}).

While the ice fall speed method of Heymsfield and Westbrook (2010) appears more accurate, the method of Mitchell (1996) yields fall speeds within ~ 10% of those based on Heymsfield and Westbrook (2010) for ice particles found in cirrus clouds (Mitchell et al., 2011). This is because ice particles in cirrus clouds generally have irregular "blocky" shapes with relatively high area ratios (defined as ice particle projected area divided by area of circle having the same maximum dimension), with aspect ratios relatively close to unity. For such ice crystals (T < -38°C), the difference in fall speeds between schemes is minimal (Heymsfield and Westbrook, 2010), ~ 10% or less based on Mitchell et al. (2011). To correct for this overestimation, the fall speeds predicted by (13) and (14) are multiplied by 0.90 to bring them closer to Heymsfield-Westbrook (2010) values.

https://doi.org/10.5194/acp-2020-846
Preprint. Discussion started: 22 October 2020

Atmospheric Chemistry and Physics Discussions

The result of this methodology for V_N is shown in Fig. 2. The procedure described above generated the orange data points shown, relating D_{mean} to V_N. This data was then approximated by a 2nd order polynomial curve-fit, shown by the black curve in Fig. 2, having the equation:

$$\ln(V_N) = -6.241 + 2.713 \ln(D_{mean}) - 0.1716 [\ln(D_{mean})]^2, \quad (20)$$

where D_{mean} is in microns and V_N is in cm s^{-1}. Equation (20) is used in the modified MG2 scheme for both cloud ice and snow since λ_i and λ_s are identical to force conformity with CALIPSO retrieved D_e (for cirrus clouds only).

The result of this same methodology for V_m is shown in Fig. 3. Again, the data generated from the above methodology are indicated by the orange circles, while the black curve is the curve-fit having the form:

$$\ln(V_m) = -4.484 + 1.809 \ln(D_e), \quad (21)$$

where D_e is in microns and V_m is in cm s^{-1}. Both Eqns. (20) and (21) assume reference conditions of p = 850 hPa and T = 273 K, which is also assumed in the MG2 scheme. The linear curve fit in Fig. 3 ignores the first two data points (smallest D_e) where D_e is smaller than any of the CALIPSO retrieved D_e values. This was done to reduce computation time while maintaining the same accuracy (since D_e is restricted to the range of retrieved median D_e values). Nonetheless, the following line equation fits all the data points in Fig. 3, with improved accuracy for the smallest D_e:

$$\ln(V_m) = -5.059 + 2.079 \ln(D_e) - 0.03119 [\ln(D_e)]^2. \quad (22)$$

Note that Eq. (21) has the simple form

$$V_m = 0.01129 D_e^{1.809}. \quad (23)$$

Again, D_e is in microns and V_m is in cm s^{-1}, and assumed reference conditions are p = 850 hPa and T = 273 K.

These formulations for V_N and V_m are compared with V_N and V_m determined by other studies in Fig. 4. The ice fall speed schemes compared are from the MG2 scheme, from Mishra et al. (2014) and from Heymsfield and Westbrook (2010). While V_N and V_m are PSD integrated values in the current treatment, in Mishra et al. (2014) and in MG2, the treatment for the Heymsfield-Westbrook scheme is based on D_{mean} and D_m, respectively. The Mishra et al. scheme generally agrees within 20% and 30% for V_N and V_m, respectively, while the Heymsfield-Westbrook scheme generally agrees with V_m within 30%.

https://doi.org/10.5194/acp-2020-846
Preprint. Discussion started: 22 October 2020

Atmospheric Chemistry and Physics Discussions

2.3 Calculation of cirrus cloud ice particle number concentration

Using the cloud ice number concentration N_i and λ from the last time step, the MG2 microphysics determines the cloud ice water content (IWC), or, in MG2 terms, the mass mixing ratio for cloud ice, and similarly for calculating the mass mixing ratio for snow. In the modified MG2 scheme, N_i and N_s (number concentration for snow) are determined through the mass balance relationship for the assumed gamma PSD (Mitchell et al., 2006, Eq. 29):

$$N = \frac{IWC\ \lambda^{\beta}}{\alpha\,\Gamma(\beta+1)} = \frac{\rho_{air}\,q_{ice}\,\lambda^{\beta}}{\alpha\,\Gamma(\beta+1)}, \quad (24)$$

where ρ_{air} = air density in kg/m^3 and q_{ice} is the ice mixing ratio (either for cloud ice or snow) in kg/kg. The MG2 scheme provides an initial estimate of nucleated ice embryos from which an initial q_{ice} is estimated. But thereafter, λ is given by Eq. (7) and N_i and N_s are calculated from Eq. (24). In this way, "ice nucleation" is driven by the CALIPSO D_e retrievals via Eq. (24), eliminating most of the uncertainty associated with N ($N_i + N_s$). Ice nucleation is poorly understood, and this approach is designed to yield a more realistic estimate of N in cirrus clouds. For realistic N values, IWC is not very sensitive to N, with the supersaturation with respect to ice, S_i, increasing when N is relatively low and decreasing when N is relatively high. These changes in S_i alter the rate of vapor deposition to ice crystals, reducing the sensitivity of IWC to changes in N.

For estimating N_i and N_s in cirrus clouds, representative values for α and β in Eq. (24) are needed regarding the cloud ice and snow fraction. For the SPARTICUS synoptic cirrus cloud dataset described in Mishra et al. (2014) and Mitchell et al. (2018, henceforth M2018), D_{mean} (in microns) can be very crudely approximated from cloud temperature (°C) using the following linear regression (which works best for T > -42°C):

$$D_{mean} = 5.09\ T + 324\ . \quad (25)$$

Figure 5 shows this SPARTICUS data along with this regression line. From Figure 5, for T < -38°C, $D_{mean} \approx 50$ μm appears reasonably representative for calculating α and β for the cloud ice fraction. From Table 1 of EM2016, assuming synoptic cirrus clouds where -55°C < T < -40°C, $\alpha = 2.8755$ (mks units) and $\beta = 2.5523$. For cirrus clouds where T < -38°C, the sedimenting mass flux (i.e. the snow fraction) will be associated with D_m, which is about 3 times larger than D_{mean} (Mitchell, 1990). Since our representative D_{mean} is 50 μm, our representative D_m is ~ 150 μm, which corresponds to $\beta = 2.2846$ and $\alpha = 0.2350$ (mks units). These values of α and β are used to calculate N_i and N_s for cloud ice and snow in Eq. (24).

The so-called PSD y-intercept parameter N_0 is used in the MG2 scheme for calculating vapor deposition/sublimation (along with λ), as well as other processes. For $\nu = 0$, it is calculated as:

https://doi.org/10.5194/acp-2020-846
Preprint. Discussion started: 22 October 2020

Atmospheric Chemistry and Physics Discussions

$$N_0 = N \lambda. \quad (26)$$

2.4 Ice particle growth processes

The above changes can affect ice particle growth/sublimation through water vapor diffusion and collection processes. In this treatment, growth and sublimation through diffusion are affected through λ and N, but collection processes (i.e. snow self-aggregation, accretion of cloud ice by snow) that have an ice fall speed dependence are not affected by these changes. Rather, the original MG2 ice fall speed parameters (*a* and *b*) are used for these collection processes. Ice fall speeds based on the original MG2 fall speed parameters for cloud ice and snow agree with this new treatment roughly within a factor of 2, and thus should be adequate for estimating removal rates of cloud ice by snow and snowfall aggregation rates. The Bergeron process subroutine was not affected since this requires mixed phase conditions (only ice exists in cirrus clouds).

For context, the accretion of cloud ice by snow in MG2 is expressed by a removal rate by snow, R_{acc}, times the IWC:

$$R_{acc} = \int_0^\infty V_s(D)\, A(D)\, E_{i,s}\, N(D)\, dD = \int_0^\infty a_s D^{b_s} (\pi/4) D^2 E_{i,s} N_{0,s} \exp(-\lambda D)\, dD = (\pi/4)\, a_s N_{0,s} E_{i,s} \Gamma(b_s + 3)/\lambda_s^{bs+3} \quad (27)$$

where V_s = snow fall speed, A(D) = projected area of snow particle, $E_{i,s}$ = collection efficiency of cloud ice by snow, and N(D) is the PSD. Note that Eq. (27) assumes $V_s >> V_i$, where V_i = fall speed of cloud ice (this may overestimate R_{cc} for cirrus clouds in the modified MG2 scheme). In this modified MG2 scheme, $\lambda_i = \lambda_s = \lambda = 1/D_{mean}$, $N_{0,i} = N_i \lambda_i$, $N_{0,s} = N_s \lambda_s$, and standard MG2 values remain for a_s and b_s, where subscripts i and s denotes the cloud ice and snow fraction, respectively. Since IWC = $\rho_a q_i$, where ρ_a = air density and q_i = cloud ice mixing ratio, the mass accretion rate is R_{acc} × IWC and the N accretion rate is R_{acc} N.

2.5 Smoothing D_e transitions

As mentioned, the CALIPSO D_e retrievals were partitioned into 24 latitude and seasonally dependent categories over land and 24 of such categories over ocean in the modified MG2 scheme. Sudden D_e differences can sometimes occur across category boundaries unless some kind of smoothing algorithm is applied. To smooth D_e transitions across categories, two latitudes were defined that were ± 5° latitude from the latitude being solved for, and the D_e subroutine then yielded D_e values for these two latitudes. We now have two D_e values and two latitude values from which to define a line equation, which is used to calculate the original D_e (between these two latitudes). This procedure prevents any sudden jumps in D_e value from occurring and produces a D_e gradient over 10° latitude.

https://doi.org/10.5194/acp-2020-846
Preprint. Discussion started: 22 October 2020


Atmospheric Chemistry and Physics Discussions

2.6 Preparation of CALIPSO D_e data and a MG2-CALIPSO subroutine for D_e

The D_e subroutine in the modified MG2 scheme provides cirrus cloud D_e values at 4 K temperature resolution for 168 K ≤ T ≤ 268 K, but D_e was not sampled across this entire temperature range. The D_e values beyond the minimum and maximum sampled D_e take on the value of the minimum and maximum sampled D_e, respectively. Appendix A contains a more detailed account describing how unsampled D_e values were interpolated or extrapolated from the sampled D_e. The D_e subroutine (in Fortran90) used in MG2/WACCM6 that contains the LUTs giving D_e as a function of T for each D_e category (that are functions of season, latitude and ocean vs. land) is provided as a supplement to this manuscript as a possible resource to investigators who would like to pursue this type of research. An explanation of the subroutine is also provided.

3 Experimental design

As mentioned, this study uses CALIPSO D_e retrievals to constrain PSDs and ice fall speeds in WACCM6. These retrievals apply to single layer cirrus clouds having an OD range from 0.3 to 3.0. As explained in Sect. 6.3 of M2018, cirrus clouds in this OD range should dominate the overall cirrus cloud net radiative forcing, making their cloud properties relevant to climate modeling experiments that seek to understand cirrus cloud radiative effects.

In order to evaluate the radiative effect of hom relative to het, a second modified version of the MG2 scheme was produced that estimates cirrus cloud microphysical properties resulting from het. This second version is the same as the first modified version described in Sect. 2 with the exception that the CALIPSO D_e – T relationships obtained from the tropics (± 30° latitude) are applied globally. That is, for a given T, the D_e for latitude zones 0 – 30 N and 0 – 30 S are averaged for each season, and the resulting LUTs for ± 30° latitude are applied to all six 30° latitude zones. This was done since retrieved N was lowest (~ 50 to100 L^{-1} based on the retrieval version most valid for the tropics; see M2018, Fig. 12b) in this ± 30° latitude zone relative to N at latitudes outside this zone, suggesting that the corresponding tropical D_e would be the most representative of D_e from cirrus clouds formed via het. For this reason, the WACCM6 simulation corresponding to this second modified version of MG2 is referred to as HET. Although mechanisms/processes other than het may be responsible for N in the tropics (e.g. Lawson et al. 2015; 2017), similar low or minimal N are retrieved for regions outside the tropics where het likely dominates. But such regions outside the tropics are not as spatially extensive as the tropics, making the tropics the most convenient region for developing "het" D_e – T relationships.

In total, this modeling experiment consists of three 40-year simulations that are based on standard WACCM6, WACCM6 using the modified MG2 scheme as described in Sect. 2, and the HET version of WACCM6 as described above. Henceforth, these simulations will be referred to as WACCM, CALCAL (for calibrated with CALIPSO D_e) and HET, as shown in Table 1. The "specified chemistry" version of WACCM6 (which runs faster than the

https://doi.org/10.5194/acp-2020-846
Preprint. Discussion started: 22 October 2020

Atmospheric Chemistry and Physics Discussions

complete WACCM6) is used here since this study is not expected to be sensitive to changes in atmospheric chemistry. The default ice nucleation scheme of Liu and Penner (2005) is used in WACCM, where the pre-existing ice option is switched on. This option enhances the influence of het, reducing N by a factor of ~ 10 in the mid- to high latitudes (Shi et al., 2015). Differences between CALCAL and WACCM are intended to reveal deficiencies in the treatment of ice nucleation in the MG2 scheme, while differences between CALCAL and HET are intended to estimate the microphysical and radiative contribution of hom in natural cirrus clouds. The simulation period is 1975-2014. The horizontal resolution is 0.9° latitude × 1.25° longitude, and there are 70 vertical levels. Climatological sea surface temperatures are used, which neutralize potential feedback effects from the ocean. Each simulation is "spun-up" to achieve balanced (stable) initial conditions before the simulation period commences.

As described in M2018, one has a selection of CALIPSO retrieval formulations to choose from; (1) based on SPARTICUS in situ data with the smallest size-bin of the 2D-S probe [$N(D)_1$] included; (2) same but not including $N(D)_1$; (3) based on TC4 in situ data with $N(D)_1$ included; (4) same but not including $N(D)_1$. It was found in M2018 that formulations (1) and (2) yielded comparable agreement in the temperature dependence of β_{eff} obtained from two methods; direct measurement of β_{eff} by CALIPSO IIR during SPARTICUS (considered most reliable) and calculation of β_{eff} from SPARTICUS PSD measurements. Since the SPARTICUS field campaign was conducted in the central United States (over or near the Rocky Mountains and often over low-lying plains), this suggests that either retrieval formulation (1) or (2) may yield realistic retrievals outside the tropics, but formulation (1) yielded superior agreement with in situ D_e measurements during SPARTICUS. The TC4 field campaign was conducted in the tropics near Costa Rica, usually over ocean. As described in M2018, formulation (4) produced the best agreement in the temperature dependence of β_{eff} obtained from the above two methods (i.e. direct measurement of β_{eff} by CALIPSO IIR during TC4 and calculation of β_{eff} from TC4 PSD measurements). In this modeling study, we used formulation (1) outside the tropics and formulation (4) within the tropics. Differences in D_e between formulations (1) and (4) are shown in Fig. 11 of M2018.

3.1 Seasonality of cirrus cloud properties

Although based only on formulation (1) of the CALIPSO retrieval (which produces the highest N), Figs. 6 and 7 show the seasonal dependence of global distributions of median D_e and median N for 2008 and 2013, which is represented in the LUTs regarding the former. The seasonal dependence of N shown in Fig. 7 was also found by Sourdeval et al. (2018) at mid-to-high latitudes for winter vs. summer. Ice-supersaturated regions (ISSRs) are requisite for cirrus cloud formation, and between the tropopause and ~ 100 hPa below that level and between 40 and 60° N. latitude, observations of RHi and ISSR frequency exhibit a clear seasonal dependence, being highest during winter (DJF) and lowest during summer (Petzold et al., 2020). Since higher RHi may coincide with more frequent incidences of hom, these RHi and ISSR observations appear to support the findings in Figs. 6 and 7 (assuming

https://doi.org/10.5194/acp-2020-846
Preprint. Discussion started: 22 October 2020


Atmospheric Chemistry and Physics Discussions

higher N is associated with more frequent incidences of hom). Additional evidence for this seasonality can be found in the cirrus cloud reflectance measurements of Zhao et al. (2020), where reflectance from cirrus clouds is highest during winter and lowest during summer at mid-to-high latitudes.

As described in M2018 and shown in Figs. 6 and 7, D_e is smaller and N is higher over mountainous terrain. This is likely due to greater contributions from hom that occur in sustained updrafts from low frequency gravity waves induced by the mountains. This was also observed (and explained similarly) in the remote sensing study by Gryspeerdt et al. (2018). During winter, there is less mixing from deep convection, which may reduce INP concentrations in the upper troposphere, allowing the RHi threshold for hom to be more frequently realized.

4 Comparisons of CALIPSO retrievals with an in situ cirrus cloud climatology

Although CALIPSO retrievals of D_e, N and IWC are compared against corresponding in situ measurements from three field campaigns in M2018, a recent study by Krämer et al. (2020) has expanded the in situ cirrus cloud property database described in Krämer et al. (2009) by a factor of 5 to 10 (depending on cloud property). Here we convert CALIPSO retrievals of D_e to the spherical volume radius (R_v) of the mean ice particle mass, IWC/N, and compare the temperature dependence of this "retrieved" R_v with the in situ R_v from the Krämer et al. (2020) climatology. To facilitate comparisons between model-predicted N and in situ N, in Appendix B, N is calculated for exponential gamma PSD (Eqn. 6) based on in situ R_v and IWC climatology as a function of T and compared with the in situ N reported in Krämer et al. (2020). This N is denoted as N_{calc}. This same method is applied in Appendix B to calculate N based on retrieval-derived R_v and climatological in situ IWC. This N, denoted N_{CAL}, is thus the N consistent with retrieved D_e and climatological IWC. Comparisons between in situ N, N_{calc} and N_{CAL} are shown in Fig. B2 of Appendix B.

As stated in Krämer et al. (2020), the influence of wave cirrus clouds in the lee of Norwegian mountains was diminished in this new dataset, with most flights over lowlands and ocean (see Fig. 1 of that paper). As shown and discussed in Gryspeerdt et al. (2018), M2018 and Figs. 6-7, relatively high N and small D_e are associated with mountainous topography, suggesting an enhanced contribution from hom; the opposite was observed over ocean and lowlands. To compare the M2018 D_e with in situ R_v from Krämer et al. (2020), D_e retrieved over ocean in the tropics (± 30 °latitude) is averaged with D_e over ocean in the Northern Hemisphere midlatitudes (30 °N – 60 °N). Since the Krämer et al. (2020) data has no seasonal dependence, retrieved D_e is averaged over all seasons. Figure 3 in Krämer et al. (2020) shows that very few R_v measurements were made in the Arctic, and the few that were made are near 60 °N latitude, which is why retrieved D_e is restricted to the tropics and midlatitudes.

The relationship between R_v and D_e can be evaluated numerically by incrementing D_{mean} and calculating D_e by inverting Eq. (1) and calculating R_v from:

https://doi.org/10.5194/acp-2020-846
Preprint. Discussion started: 22 October 2020

Atmospheric Chemistry and Physics Discussions

$$R_v = [3\ IWC/(4\ \pi\ \rho_i\ N)]^{1/3} = [3/(4\ \pi\ \rho_i)]^{1/3}\ (IWC/N)^{1/3}\ . \quad (28)$$

This calculation assumed a gamma exponential PSD as defined by Eq. (6) with ν = 0, with ice particle m and A defined by Eqns. (2) and (3) and calculated using the EM2016 relationships described in Sect. 2.1. For a given IWC, N was calculated via Eq. (24). R_v is related D_e in this way in Fig. 8, shown by the red diamond symbols. Also shown in Fig. 8 are curve fits relating R_v to D_e based on Eqns. (28) and (12), where N, A_{PSD} and IWC come from 2D-S (two-dimensional stereo) probe PSD measurements during the SPARTICUS and TC4 field campaigns (described in M2018). These in situ calculations are shown by the blue squares in Fig. 8. The curve fit equations are given in Appendix B. It was found that the R_v-D_e relationship is sensitive to ν, and the closer the curve fit is to the red diamond symbols, the more the measured PSD conform to exponential PSD. Due to this sensitivity to PSD shape, in situ measurements were used to define the R_v-D_e relationship, using the TC4 curve fit when D_e was retrieved from the tropics and the SPARTICUS curve fit for the midlatitudes.

The results of this analysis are shown in Fig. 9 where R_{ice} (same as R_v) is plotted against sampling temperature for the in situ climatology (black curve) and the D_e-derived R_v values (blue curves). The blue-dotted curve gives the overall R_v averaged over the tropical and midlatitude oceans. The dashed blue curve gives R_v for the tropical oceans only; recall that the HET simulation is based on the D_e – T relationships from the tropics since this is where N was consistently lowest and D_e largest, and thus representative of cirrus formed through het. A potential explanation for the relative agreement between the dashed-blue curve and the black curve is that primarily het-dominated cirrus clouds were sampled in Krämer et al. (2020). The elevated portion of the black curve between 208 K and 190 K is not observed in either of the two D_e-derived curves based on two years of CALIPSO retrievals. This may be due to limited in situ sampling over this temperature range since the numerous retrievals here should capture the temperature trend of D_e. The dotted blue curve is below the dashed blue curve because D_e tends to be smaller at midlatitudes relative to the tropics.

A more detailed analysis is given in Appendix B where N is calculated from the in situ median IWC and R_v given in Krämer et al. (2020) based on Eq. (6) and exponential PSD (ν = 0). This calculated N is appropriate for comparing with N predicted from the MG2 scheme that uses these PSD assumptions. In addition, using the comparison in Fig. 9 between 208 K and 235 K where the R_v trend with temperature is similar between the black and blue-dotted curves, it was found that on average, overall retrieved R_v was ~ 80% of the median in situ R_v. It is natural to ask what this retrieved R_v implies in terms of a N – T climatology, and how this climatology compares with other N – T climatological measurements. Using this percentage to estimate retrieved R_v from in situ median R_v, along with the in situ median IWC, N was calculated as a function of temperature. As shown in Fig. B2 of Appendix B, this temperature dependence of N is similar to the N – T dependence reported in Fig. 4 of Gryspeerdt et al. (2018).

https://doi.org/10.5194/acp-2020-846
Preprint. Discussion started: 22 October 2020


Atmospheric Chemistry and Physics Discussions

5 Modeling results and discussion

Figures 10 and 11 show global distributions for annual means regarding D_e and N (the in-cloud values) at 250 hPa, respectively, as predicted by the CALCAL, WACCM and HET simulations. The 250 hPa level is associated with lower cirrus (near 235 K) in the tropics (± 30° latitude) and mid-to-high level cirrus at high latitudes. Since D_e generally decreases with T, this contributes to the decrease in D_e at higher latitudes. But since the CALCAL model simulation is based on D_e in Fig. 6 showing a poleward decrease in D_e (averaged over all T < 235 K), this is also partly responsible for the poleward decrease in D_e in Fig. 10 regarding CALCAL, which shows the lowest D_e outside the tropics. Cirrus cloud N in Fig. 11 is relatively high in CALCAL and HET relative to WACCM, being highest in CALCAL, and thus inversely proportional to relative changes in D_e shown in Fig. 10. However, N also depends on IWC, and higher than climatological IWCs could also contribute to relatively high N. For example, Fig. B2 indicates that N based on climatological IWCs and retrieved D_e should generally range between 50 and 400 L^{-1}. The frequent prediction of N > 300 L^{-1} suggests that predicted IWCs are high relative to the in situ climatology. On the other hand, predicted N in CALCAL is broadly consistent with retrieved N in Fig. 7, which (as mentioned above), corresponds to relatively thick cirrus that are most relevant to radiation transfer. As predicted by Eq. (24), N in the tropics is relatively high where the IWC tends to be higher, such as along the ITCZ, the western tropical Pacific Ocean, Polynesia, the Amazon Basin and the Congo. Possibly because the D_e subroutine in the modified MG2 scheme is not sensitive to land topography, N in Fig. 11 is not relatively high over mountainous terrain like the retrieved N is in Fig. 7. In regards to Figs. 6 and 7, D_e tends to be larger and N lower outside the tropics during the summer season. This behavior (not shown) was captured in the CALCAL simulation.

WACCM – CALCAL and HET – CALCAL differences are shown in Fig. 12 for the annual means of D_e and N. Outside the tropics, WACCM – CALCAL D_e differences are up to ~ 100 µm whereas HET – CALCAL D_e differences are up to ~ 20 µm. Within the tropics, HET – CALCAL D_e and N differences are near zero due to the design of this experiment (D_e in the tropics in HET and CALCAL is the same). While WACCM N is almost always less than CALCAL N, over the tropical oceans these N differences are relatively small but still substantial. Outside the tropics, especially along the storm tracks, CALCAL N can be up to ~ 150 L^{-1} higher relative to HET N (presumably due to hom), and up to ~ 400 L^{-1} higher relative to WACCM. These N differences are largest during the winter season (not shown).

5.1 Cloud micro- and macrophysical HET – CALCAL differences

Since this study is on homogeneous ice nucleation, the HET – CALCAL differences will be the focus henceforth. One of the most surprising results of this study was the impact of cirrus clouds on the mixed phase cloud layer below them. The upper panel in Figure 13 shows the dependence of HET – CALCAL D_e zonal mean differences on pressure and latitude. Since D_e in the ± 30° latitude zone is treated the same in HET and CALCAL, differences are

https://doi.org/10.5194/acp-2020-846
Preprint. Discussion started: 22 October 2020


Atmospheric Chemistry and Physics Discussions

near zero within this zone. All differences are positive (shown by reddish tones) and only the upper portion corresponds to cirrus clouds. For example, in Fig. 12, the 250 hPa HET – CALCAL D_e differences are typically ~ 12 μm in the NH, but Fig. 13 shows much larger D_e differences below this cirrus cloud layer that correspond to the zone of mixed phase clouds. This larger D_e difference appears to result partially from differing fluxes of sedimenting ice particles from overlying cirrus clouds and partially from differences in ice fall speeds. In the former, assuming sedimenting cirrus ice crystals contribute substantially to N in the mixed phase zone, N in this zone should be lower in the HET simulation, with less competition among ice particles for water vapor (i.e. RHi will be higher), with individual ice particles growing larger. In the latter, ventilation effects on diffusional growth (which can more than double stationary diffusional growth rates) are stronger at higher ice fall speeds, increasing D_e in the mixed phase zone. Higher ice fall speeds also increase collision kernels for aggregation and riming, increasing those respective growth rates. The higher growth rates from all these processes further increase fall speeds, allowing D_e to increase synergistically in the mixed phase zone.

A similar pattern is seen in the lower panel of Fig. 13, which shows HET – CALCAL zonal mean differences for the ice mass mixing ratio. This is always negative due to lower N in the HET simulation, which is due to a lower flux of sedimenting cirrus ice particles and the higher fall speeds of larger ice particles. These differences often constitute a 10% decrease or more relative to CALCAL.

HET – CALCAL differences in cloud fraction are shown in Fig. 14 (upper panel). The cirrus cloud zone is characterized by a decrease in cloud fraction relative to CALCAL, due to higher fall speeds in HET. That is, the flux of ice from the base of a cirrus cloud strongly affects its lifetime and thus cloud fraction (e.g. Mitchell et al., 2008). This enhanced export of ice from the cirrus zone lowers the RHi in the upper troposphere (lower panel), but this ice export increases the RHi in mixed phase zone, which increases cloud lifetime and thus cloud fraction there. The percent RHi changes in the mixed phase zone are generally greater than the changes in the cirrus cloud zone. This is also true for cloud fraction in the Northern Hemisphere (NH).

5.2 Understanding the CRE differences

The cloud radiative effect or CRE is defined as the sum of the top-of-atmosphere (TOA) net longwave (LW) and net shortwave (SW) cloud radiative effects, denoted LWCRE and SWCRE in Table 2. Also in Table 2 are the TOA net LW and SW fluxes for all sky conditions (that include clouds), denoted FLNT and FSNT. If these same TOA net fluxes for clear sky conditions (i.e. no clouds) are denoted as FLNTC and FSNTC, respectively, then LWCRE = FLNT – FLNTC and SWCRE = FSNT – FSNTC, and CRE = LWCRE + SWCRE. The performance of WACCM6 is documented in Gettelman et al. (2019), and as a check on the integrity of model output, Table 2 compares FLNT, FSNT, LWCRE and SWCRE from our 40-year WACCM simulation with the corresponding WACCM6 variables reported in Table 3 of Gettelman et al. (2019), as well as their observed values (also taken from this Table 3). Table

https://doi.org/10.5194/acp-2020-846
Preprint. Discussion started: 22 October 2020


Atmospheric Chemistry and Physics Discussions

2 shows that the 40-year simulation values are very close to those reported in Gettelman et al. (2019), indicating these fluxes are accurate.

Table 3 shows the CRE differences regarding the WACCM, CALCAL and HET simulations. Although the MG2 scheme was only changed for $T \leq 235$ K, the CRE differences are substantial due to D_e changes in the mixed phase zone (described above). The CRE for ice clouds depends strongly on the cloud optical thickness τ and the cloud fraction, where at solar wavelengths,

$$\tau = 3\ IWP/(\rho_i\ D_e)\ , \qquad (29)$$

where IWP is the ice water path and ρ_i is the bulk density of ice (e.g. Mitchell, 2002). With generally larger D_e and lower IWP in the HET simulation, τ tends to be lower in HET relative to CALCAL. If cloud fraction stays constant, this would result in lower SWCRE and LWCRE in HET. But the radiative effects resulting from changes (HET – CALCAL) in the upper- and mid-level cloud fraction adds complexity to the calculation of CRE. The combined effect is a more negative HET net CRE relative to CALCAL, as shown in Fig. 15 and Table 3. The HET – CALCAL CRE difference has a strong seasonal dependence, as shown in Fig. 15, where ΔCRE is as large as -5 W m^{-2} over large regions at winter latitudes.

The reason the HET – CALCAL CRE difference is substantial at higher latitudes relates to the dependence of absorbed solar radiation and outgoing longwave radiation (OLR) on latitude and season. The annual average of these two fluxes is equal around ± 38 °latitude (Petty, 2006), with OLR dominating at higher latitudes. During winter, this OLR dominance increases and decreases during summer due primarily to the changing noontime solar zenith angle. Since cirrus clouds absorb LW radiation more efficiently than they reflect SW radiation, the cirrus CRE is determined primarily by OLR which dominates the radiation budget most at high latitudes during winter. At lower latitudes, SWCRE and LWCRE in cirrus clouds are comparable and tend to cancel so that the HET – CALCAL CRE is minimal. All this accounts for the latitude and seasonal dependence in Fig. 15.

While the HET – CALCAL CRE differences outside the tropics are considerable in Table 3 (-2.37 W m^{-2} for the N.H. and -2.55 W m^{-2} for the S.H.), the global mean CRE difference is considerably less (-1.16 W m^{-2}). This is because in the ± 30 °latitude zone, D_e – T relationships were identical in HET and CALCAL. But even if these D_e – T relationships differed, this latitude zone would contribute little to the global mean CRE difference since, as noted above, the cirrus cloud SWCRE and LWCRE tend to cancel in the tropics (Storelvmo and Herger, 2014).

5.3 TOA net radiative fluxes

In the final analysis, what matters most to climate are the differences in TOA net flux (FSNT - FLNT) between simulations; these are shown in Table 4. Although these net flux differences are mostly due to CRE differences,

https://doi.org/10.5194/acp-2020-846
Preprint. Discussion started: 22 October 2020


Atmospheric Chemistry and Physics Discussions

they are also partly due to differences in absorption/emission by water vapor that affect FLNT; we call this the relative humidity or RH radiative effect. As shown in Fig. 14, HET has relatively less cloud fraction and RH in the upper troposphere (UT) relative to CALCAL, and relatively higher cloud fraction and RH at mid-levels relative to CALCAL. However, the mid-level changes are greater than the UT changes (both in magnitude and vertical extent), which acts to reduce FLNTC more in HET. This appears to be the main cause of the difference between the CRE changes in Table 3 and the TOA net flux changes in Table 4. HET – CALCAL differences in TOA net flux are shown in Fig. 16 based on annual means and for winter verses summer. As with the CRE differences, there is a strong seasonal dependence. The RH radiative effect is strongest in the Polar Regions, especially during the N. H. summer. Table 5 shows TOA net flux differences outside the tropics, similar to Table 4, except that the summer months (JJA in the N.H. and DJF in the S.H.) are omitted from the averaging. These differences in Table 5 are greater than in Table 4 due to three factors that tend to be greater during non-summer months at these latitudes: hom contributions to cirrus formation, the dominance of OLR (relative to incoming SW) radiation, and a diminished (relative to summer) RH radiative effect that counteracts the CRE.

In addition to RH, there are other factors affecting the difference between simulations regarding TOA net flux and net CRE. The clear sky fluxes are also sensitive to aerosols, and to other radiatively active gases. Since this study uses the "specified chemistry" version of WACCM6, it is less likely that ozone and other greenhouse gas concentrations are significantly changing between simulations. Nonetheless, changing clouds will change actinic fluxes and photolysis rates, and thus reactive gas concentrations, which could also affect the clear sky fluxes. Aerosol concentrations can also be changed by modest circulation changes that change scavenging rates.

In Tables 3 and 4, since WACCM D_e > HET D_e > CALCAL D_e, one might expect the WACCM – CALCAL radiation differences to exceed the HET – CALCAL differences. But these differences also depend on the cloud IWC, and IWCs could be higher in WACCM at least partly because WACCM ice fall speeds tend to be lower than those in HET and CALCAL; see Fig. 4. Note that ice fall speeds can strongly impact IWCs (Mitchell et al., 2008).

6 Conclusions

As discussed in M2018 and Sect. 1, and also in other recent studies (Zhao et al., 2018; Sourdeval et al., 2018; Gryspeerdt et al., 2018), homogeneous ice nucleation (hom) contributes substantially to the microphysical and radiative properties of cirrus clouds, depending on cooling rate, latitude, season and topography. Explanations for why this happens are offered in these studies and in Sect. 1, which identifies two fundamental reasons: (1) higher cooling rates (updrafts) in mountain-induced waves and (2) the hom RHi threshold is more easily reached when INP concentrations are relatively low. In addition, INP concentrations at cirrus levels probably depend on deep convection, which occurs much more often during summer. Also, pre-existing ice advected into anvil cirrus competes effectively for water vapor, suppressing RHi and reducing the frequency of hom. These may be the

https://doi.org/10.5194/acp-2020-846
Preprint. Discussion started: 22 October 2020

Atmospheric Chemistry and Physics Discussions

reasons that, outside the tropics, D_e tends to be largest and N lowest during the summer season as shown in Figs. 6 and 7. The seasonal behavior of D_e and N shown in Fig. 6 and 7 is probably not sufficiently realized in climate models. This study attempts to estimate the radiative impact of this seasonal behavior.

From the HET – CALCAL differences in Table 3, one can infer that the CRE is sensitive to hom, and that the hom CRE effect is large enough to affect climate. For example, it is possible that climate sensitivity depends on INP concentration, where climate sensitivity is the global mean change in surface temperature resulting from a doubling of CO_2 at radiative equilibrium. If an increase in INP concentration were to neutralize the hom CRE effect, then it is possible that this could significantly decrease the global mean surface temperature. However, to adequately test this hypothesis, fully coupled simulations would be needed (i.e. these are atmosphere global climate model simulations).

Many attempts to estimate the radiative contribution of hom (relative to het) were addressing the efficacy of the climate intervention method often referred to as cirrus cloud thinning or CCT (e.g. Storelvmo et al., 2013; Muri et al., 2014; Storelvmo and Herger, 2014; Storelvmo et al., 2014; Crook et al., 2015; Kristjansson et al., 2015; Penner et al., 2015; Gasparini and Lohmann, 2016; Gasparini et al., 2017; Muri et al., 2018; Gruber et al., 2019; Gasparini et al., 2020). These were mostly global climate modeling studies (Gruber et al., 2019, was a regional modeling study) that differed in their treatment of hom and het as well as other processes affecting the frequency of hom. Not surprisingly, given the multitude of variables affecting hom and het, the impact of converting hom to het through seeding the UT with efficient ice nuclei ranged from a global annual mean CRE difference of - 2.2 W m^{-2} (Storelvmo et al., 2014) to essentially no impact (e.g. Penner et al., 2015; Gasparini and Lohmann, 2016). This study estimates a global annual mean HET – CALCAL CRE difference of -1.16 W m^{-2}. However, outside the ± 30 °latitude zone, the annual mean CRE difference is -2.37 W m^{-2} in the N.H. and -2.55 W m^{-2} in the S.H., and during non-summer months when CCT is effective, the TOA HET – CALCAL net flux difference is -2.4 W m^{-2} in both hemispheres. Based on this study, CCT may have a significant cooling impact at mid-to-high latitudes, but to estimate the CCT impact on surface temperatures, coupled simulations are needed that consider feedback effects from the oceans, cryosphere and land components of the earth-system.

In addition to its relevance to CCT, this study identifies an apparent deficiency in climate modeling since the indicated radiative contribution of hom and associated heating rates at mid-to-high latitudes are currently missing in climate models that explicitly treat cirrus cloud microphysics (e.g. Gasparini and Lohmann, 2016). This can have an impact on geopotential height patterns, the storm track and precipitation patterns (Li et al., 2015; 2016; 2017). Moreover, the hom radiative effects are most pronounced at mid-to-high latitudes during winter, which may affect Arctic amplification (Holland et al., 2003) and climate tipping point phenomena (Holland et al., 2006; Notz et al., 2009). For a discussion on a possible linkage between high latitude cirrus clouds and midlatitude weather, see Sect. 6.5 of M2018.

https://doi.org/10.5194/acp-2020-846
Preprint. Discussion started: 22 October 2020


Atmospheric Chemistry and Physics Discussions

Finally, this study indicates that changes in cirrus cloud D_e and N produce large consequences in the underlying mixed phase clouds and relative humidity field as described in Sect. 5.1. These consequences contribute strongly to the CRE and the TOA net radiative fluxes. More research on the microphysical processes producing these changes in mixed phase cloud properties may be needed to corroborate these findings. Note that changes to the MG2 scheme were only made for cirrus clouds where $T \leq 235$ K.

As mentioned, the atmospheric simulations in this study were not coupled with other components of the earth-system, such as the oceans, land and cryosphere, thus preventing important climate feedbacks from occurring that affect the general circulation and surface temperatures. Future research should conduct such coupled simulations to understand how potential changes in INP concentration could affect the Earth's climate. Moreover, there are four versions of the CALIPSO retrieval for D_e and N, where N can vary by about a factor of two, depending on which version is used (M2018). This modeling study could be repeated using different retrieval versions to characterize the uncertainty associated with the results reported here.

https://doi.org/10.5194/acp-2020-846
Preprint. Discussion started: 22 October 2020

Atmospheric Chemistry and Physics Discussions

Appendix A: Methodology for preparing D_e – T LUTs for the modified MG2 scheme

A new subroutine in the modified MG2 scheme relates a retrieved median D_e to a given temperature (T), latitude, season and land fraction using look-up-tables (LUTs). Each LUT consists of an array of D_e values corresponding to T at 4 K intervals, where the T range is from 168 – 268 K. However, the T range of retrieved D_e is from 188 – 235 K since only cirrus clouds are targeted by the retrieval. Interpolation is used within the cirrus T range to calculate D_e when T lies within a prescribed 4 K interval. The following guidelines were adopted for assigning D_e values in LUTs for T having no corresponding CALIPSO satellite D_e measurement or for identifying/replacing unrealistic D_e values. These selection rules assume D_e decreases with decreasing T; D_e violating this trend are usually based on a relatively small number of samples. See Fig. 11 in M2018 for graphical displays of D_e – T data used to create LUTs.

1) If retrieved median D_e corresponding to the highest T is lower than the adjacent D_e (at lower T), set D_e for the highest T equal to the adjacent D_e (producing two equal-valued D_e for the two warmest T points).

2) If retrieved median D_e for the lowest T is higher than the adjacent D_e (at higher T), set D_e for the lowest T equal to the adjacent D_e (producing two equal-valued D_e for the two coldest T points).

3) If median D_e for the two lowest T appear non-physical (i.e. they usually follow a negative slope and have D_e values larger than D_e for the 3rd lowest T), then assign them the D_e value of the 3rd lowest T if the number of samples corresponding to these two anomalous D_e is < ~ 100. Number of D_e values affected = 4.

4) When number of samples N < 10 and the median D_e is anomalous relative to adjacent values, interpolate between two adjacent D_e values to obtain the intermediate value. Number of D_e values affected = 3.

5) If median D_e for the highest T is more than 20 μm higher than the adjacent D_e-T point, and N < 10, then set the D_e for the highest T as equal to the adjacent D_e (producing two equal-valued D_e for the two warmest T points). Number of D_e values affected = 3.

Appendix B: Calculating N from retrieval-derived R_v and in situ climatology IWC

This appendix first provides the curve fit equations used in Fig. 8 to convert retrieved D_e to R_v, and then proceeds to describe a methodology for calculating N from R_v and IWC. Regarding the latter, first the in situ R_v is used, followed by R_v estimated from the median D_e retrievals averaged from the tropics and midlatitudes. The purpose of this exercise was to first calculate in situ climatological values for N (denoted N_{calc}) that conform to assumptions in

https://doi.org/10.5194/acp-2020-846
Preprint. Discussion started: 22 October 2020


Atmospheric Chemistry and Physics Discussions

climate models, such as an analytical exponential gamma function which is the case here. The second purpose was to calculate N based on retrieved D_e and in situ climatological IWCs that should provide climatological values for N that are consistent with these two climatological properties (D_e and IWC). This retrieval-derived N, denoted N_{CAL}, can then be related to other in situ and satellite climatologies of N.

B1 Curve fits used in Figure 8

As mentioned, D_e retrievals at midlatitudes utilize the SPARTICUS unmodified PSD version of this retrieval primarily because this version yielded the best agreement between retrieved and in situ D_e in retrieval validation studies (M2018). In the tropics, D_e retrievals utilize the TC4 $N(D)_1 = 0$ version of this retrieval (where $N(D)_1$ denotes the number concentration in the smallest size bin of the 2D-S probe) because the CALIPSO IIR measurement of the temperature dependence of β_{eff} (the 10.6 to 12.05 μm effective absorption optical depth ratio) matched β_{eff} derived from in situ PSD measurements the best when $N(D)_1 = 0$. These same microphysical assumptions were adhered to (unmodified PSD for SPARTICUS and $N(D)_1 = 0$ for TC4) when producing the curve fits shown below. The SPARTICUS curve fit shown in Fig. 8 is a 6-order polynomial function for $D_e \geq 45$ μm and a linear extrapolation for $D_e < 45$ um. For $D_e \geq 45$ um,

$$R_v = a_0 + a_1 D_e + a_2 D_e^2 + a_3 D_e^3 + a_4 D_e^4 + a_5 D_e^5 + a_6 D_e^6, \quad \text{(B1)}$$

with $a_0 = 33.2197$, $a_1 = -4.33987$, $a_2 = 0.261068$, $a_3 = -0.00712459$, $a_4 = 9.93114e-05$, $a_5 = -6.65497e-07$ and $a_6 = 1.69976e-09$, where units are microns. For $D_e < 45$ um,

$$R_v = 0.310553 (D_e - 45) + 15.9104, \quad \text{(B2)}$$

where again units are microns. The linear extrapolation is well adapted in the range of D_e that we observe.

For the TC4 curve fit shown in Fig. 8,

$$R_v = a_0 + a_1 D_e + a_2 D_e^2 + a_3 D_e^3, \quad \text{(B3)}$$

where $a_0 = 5.58658$, $a_1 = 0.290955$, $a_2 = -0.00266899$ and $a_3 = 5.51555e-05$ and units are microns. For $D_e < 18$ μm,

$$R_v = 0.5598 D_e. \quad \text{(B4)}$$

B2 Methodology for calculating N from in situ R_v and IWC

The same curve-fitting methodology described above was applied here in relating the dependent variable D_e to the independent variable R_v, where R_v comes from the in situ climatology of Krämer et al. (2020). In Sect. B1 the goal was to obtain R_v from retrieved D_e for the purpose of comparison with in situ R_v in Fig. 9. In this section, the goal is

https://doi.org/10.5194/acp-2020-846
Preprint. Discussion started: 22 October 2020

Atmospheric Chemistry and Physics Discussions

to obtain D_e from in situ R_v (or an estimate of retrieved R_v from in situ R_v), and then estimate N from this D_e and the in situ climatology IWC. The $D_e - R_v$ curve fit for the midlatitudes using SPARTICUS data is shown in Figure B1 (black curve) for T < 235 K and is described mathematically with micron units as

$$D_e = -11.6202 + 4.09910\ R_v + 0.00767864\ R_v^2 - 0.00371768\ R_v^3 + 8.72769e\text{-}05\ R_v^4 - 8.01817e\text{-}07\ R_v^5 + 2.64619e\text{-}09\ R_v^6. \quad \text{(B5)}$$

For R_v < 5 μm, D_e is given by

$$D_e = 1.7309\ R_v. \quad \text{(B6)}$$

The $D_e - R_v$ curve fit for the tropics (± 30 °latitude) using TC4 data is shown in Figure B1 (black curve) for T < 235 K and is described mathematically with micron units as

$$D_e = -25.4617 + 5.00679\ R_v - 0.0709877\ R_v^2 + 0.000354202\ R_v^3. \quad \text{(B7)}$$

For R_v < 10 μm,

$$D_e = 1.7862\ R_v. \quad \text{(B8)}$$

These relationships account for PSD shape effects in anvil cirrus (sampled during TC4) and in synoptic (non-anvil) cirrus (sampled during SPARTICUS), which are assumed to be representative of PSD shape effects encountered in tropical and midlatitude cirrus analyzed in Krämer et al. (2020), respectively. Again, the red diamonds in Fig. B1 were derived from (1) and (28) using the m-D and A-D relationships in EM2016 for synoptic cirrus clouds between -40 °C and -55 °C (described in Sect. 2.1), and assuming exponential gamma PSD. Differences between these D_e-R_v values and the curve fits are believed to result from PSD shape differences that can have a large impact on N.

To obtain the final D_e that represents in situ sampling in both the tropics and midlatitudes, these two D_e values, one from the SPARTICUS relationship and one from the TC4 relationship, are averaged together. Equation (7) is then applied, which assumes exponential gamma PSD, to obtain D_{mean}. For exponential PSD, the slope parameter $\lambda = 1/D_{mean}$. From λ and the median in situ IWC reported in both Krämer et al. (2009) and Krämer et al. (2020), N (denoted N_{calc}) is calculated from this in situ climatology that conforms to exponential gamma PSD. The temperature dependence of N_{calc} and in situ N reported in Krämer et al. (2020) are compared in Fig. B2. There is fairly good agreement between 244 K and 217 K, after which N_{calc} exceeds in situ N to varying degrees (up to a factor of 8). It is difficult to determine the cause of this variance, but since in situ R_v and IWC are conserved, it may relate to changes in PSD shape at the smallest ice particle sizes. For models that parameterize ice PSD using exponential gamma distributions, from a radiation purview, model-predicted climatological N comparisons against N_{calc} may be more meaningful than using the raw in situ N measurements.

B3 Methodology for calculating N from retrieval-derived R_v and in situ IWC

Over the temperature range from 235 K to 208 K in Fig. 9, the trend is similar regarding the in situ and retrieval based estimates of R_v. Thereafter, at lower T, there is an increase for in situ R_v that is not observed in retrieval-based R_v where the sampling statistics are much greater relative to in situ measurements. Since this tendency change for in situ N ~ 208 K is not found in the retrievals, it is argued that the N comparison between 208 and 235 K is more reliable for evaluating the mean difference in R_v between in situ and retrieval-based R_v. The ratio of the sum of retrieval-based to in situ R_v values between 208 and 235 K is 0.7945 (where retrieved R_v is the mean of tropical and midlatitude values). That is, retrieval-based $R_v \approx 0.8$ in situ R_v. Using this ratio, retrieval-based R_v was estimated from in situ R_v over the entire temperature range shown in Fig. 9. The rest of the procedure is the same as in Sect. B2, where D_e is estimated from retrieval-based R_v, and D_{mean} and λ are calculated from D_e via Eq. (7). From λ and the in situ IWC, N (denoted N_{CAL} for CALIPSO) is calculated. The temperature dependence of N_{CAL} is plotted

https://doi.org/10.5194/acp-2020-846
Preprint. Discussion started: 22 October 2020

Atmospheric Chemistry and Physics Discussions

along with N_{calc} and N in situ in Fig. B2. Since N_{CAL} employs the same assumptions as N_{calc} (excepting R_v), a comparison between N_{CAL} and N_{calc} is most appropriate. Between 244 K and 218 K, $N_{CAL} > N_{calc}$ by ~ 50% to 100%. For lower temperatures, N_{CAL} can be up to a factor of 3 (i.e. 200%) higher than N_{calc}. Since D_e is used to constrain WACCM6, this provides a more realistic appraisal in terms of N regarding the differences between our CALIPSO D_e retrievals and the in situ R_v measurements in Krämer et al. (2020).

It should be appreciated that N is a difficult ice cloud property to measure using probes on aircraft and can easily vary by a factor of 2 or more depending on the instrument and data processing (e.g. Korolev et al., 2011; Lawson, 2011; Korolev and Field, 2015). Moreover, N retrievals using the DARDAR method (Sourdeval et al., 2018; Gryspeerdt et al., 2018) can vary by a factor of ~ 1.7 depending on whether the small ice crystal cut-off size used for the assumed PSD shape is 5 µm or 1 µm (M2018). The temperature dependence of N_{CAL} in Fig. B2 agrees well with the temperature-variation of retrieved N in Fig. 4 of Gryspeerdt et al. (2018) which uses 5 µm as the PSD cut-off size. The retrieval method used here does not assume any small ice crystal cut-off size, it considers all detectable particles, and the method is very sensitive to small ice crystals (M2018).

The N values shown in Fig. 7 are based on the CALIPSO retrieval version that yields the highest N estimates (i.e. the SPARTICUS unmodified PSD version), and N varies by about a factor of 2 depending on which version is used. Therefore, these N estimates may be high by a factor of 2 if the version producing the lowest N estimate is most realistic. Moreover, the retrieval applies only to relatively thick cirrus clouds having optical depths between 0.3 and 3.0. These thicker cirrus may be associated with higher updrafts where the hom contribution is larger, resulting in higher N. On the other hand, such cirrus have the strongest influence on the earth's radiation budget and are thus most representative for climate modeling purposes (M2018).

https://doi.org/10.5194/acp-2020-846
Preprint. Discussion started: 22 October 2020

Atmospheric Chemistry and Physics Discussions

Code availability. The new code developed for this project is provided as a supplement (a subroutine for replacing model predicted D_e with CALIPSO retrieved D_e as a function of temperature, latitude, season and land fraction). Other new code implemented is described mathematically by the equations relating D_e to PSD slope and D_e to the number- and mass-weighted ice fall speeds in Sect. 2. Values of α and β for calculating N_i, N_s, N_{0i} and N_{0s} in cirrus clouds ($T < 235$ K) are given in Sect. 2.3.

Data availability. Access to the CALIPSO satellite data used here is described under "data availability" in M2018 and it is also available as code in the subroutine supplement described above.

Author contributions. DM conceived and directed the study and developed/implemented new code in the MG2 scheme; JM implemented new code, executed the simulations and processed model output; AG contributed the maps of D_e and N retrievals and the conversion of D_e to R_v; YT processed model output and developed some code; MK supplied the climatology of in situ cirrus cloud properties; FH participated in the debugging process.

Competing interests. The authors declare that they have no conflict of interest.

Acknowledgements. This research was supported by NASA grant NNX16AM11G and the NASA CALIPSO project. Fruitful discussions with Dr. Phil Rasch regarding these results are acknowledged and appreciated. The use of WACCM6 for this study was recommended by Dr. Julio Bacmeister and the forty-year simulation period was suggested by Dr. Andrew Gettelman (to evaluate sudden stratospheric warming event frequencies); we thank both of them for their insights and guidance. CALIPSO products are available at the Atmospheric Science Data Center of the NASA Langley Research Center and at the AERIS/ICARE Data and Services Center in Lille (France). Resources supporting this work were provided by the NASA High-End Computing (HEC) Program through the NASA Center for Climate Simulation (NCCS) at Goddard Space Flight Center.

References

Barahona, D., and Nenes, A.: Parameterizing the competition between homogeneous and heterogeneous freezing in ice cloud formation – polydisperse ice nuclei, Atmos. Chem. Phys., 9, 5933–5948, 2009.

https://doi.org/10.5194/acp-2020-846
Preprint. Discussion started: 22 October 2020

Crook, J. A., Jackson, L. S., Osprey, S. M., & Forster, P. M.: A comparison of temperature and precipitation responses to different Earth radiation management geoengineering schemes. J. Geophys. Res., 120, 9352–9373, https://doi.org/10.1002/2015JD023269, 2015.

Cziczo, D. J., K. D. Froyd, K. D., Hoose, C., Jensen, E. J., Diao, M., Zondlo, M. A., Smith, J. B., Twohy, C. H., and Murphy, D. M.: Clarifying the dominant sources and mechanisms of cirrus cloud formation. *Science*, 340, 1320-1324, 2013.

Erfani, E. and Mitchell, D. L.: Developing and bounding ice particle mass- and area-dimension expressions for use in atmospheric models and remote sensing, Atmos. Chem. Phys., 16, 4379–4400, doi:10.5194/acp-16-4379-2016, 2016.

Gasparini, B. and Lohmann, U.: Why cirrus cloud seeding cannot substantially cool the planet. J. Geophys. Res., 121, 4877-4893, https://doi.org/10.1002/2015JD024666, 2016.

Gasparini, B., Münch, S., Poncet, L., Feldmann, M., and Lohmann, U.: Is increasing ice crystal sedimentation velocity in geoengineering simulations a good proxy for cirrus cloud seeding? Atmos. Chem. Phys., 17, 4871–4885, https://doi.org/10.5194/acp-17-4871-2017, 2017.

Gasparini, B., McGraw, Z., Storelvmo, T., and Lohmann, U.: To what extent can cirrus cloud seeding counteract global warming? Environ. Res. Lett. *(*in press), https://doi.org/10.1088/1748-9326/ab71a3, 2020.

Gettelman, A. and Morrison, H.: Advanced two-moment bulk microphysics for global models. Part I: Off-line tests and comparison with other schemes, J. Climate, 28, 1268-1287, doi: 10.1175/JCLI-D-14-00102.1, 2015.

Gettelman, A., Morrison, H., Santos, S. and Bogenschutz, P.: Advanced two-moment bulk microphysics for global models. Part II: Global model solutions and aerosol-cloud interactions, J. Climate, 28, 1288-1307, doi: 10.1175/JCLI-D-14-00103.1, 2015.

Gettelman, A., Mills, M. J., Kinnison, D. E., Garcia, R. R., Smith, A. K., Marsh, D. R., Tilmes, S., Vitt, F., Bardeen, C. G., McInerny, J., Liu, H.-L., Solomon, S. C., Polvani, L. M., Emmons, L. K., Lamarque, J.-F., Richter, J. H., Glanville, A. S., Bacmeister, J. T., Phillips, A. S., Neale, R. B., Simpson, I. R., DuVivier, A. K., Hodzic, A. and Randel, W. J.: The whole atmosphere community climate model version 6 (WACCM6). J. Geophys. Res., 124, 12,380-12,403, https://doi.org/10.1029/2019JD030943, 2019.

Gruber, S., Blahak, U., Haenel, F., Kottmeier, C., Leisner, T., Muskatel, H., Storelvmo, T. and Vogel, B.: A process study on thinning of Arctic winter cirrus clouds with high-resolution ICON-ART simulations. J. Geophys. Res., 124, https://doi.org/10.1029/2018JD029815, 2019.

Gryspeerdt, E., Sourdeval, O., Quaas, J., Delanoë, J., Krämer, M., and Kühne, P.: Ice crystal number concentration estimates from lidar-radar satellite remote sensing – Part 2: Controls on the ice crystal number concentration, Atmos. Chem. Phys., 18, 14351–14370, https://doi.org/10.5194/acp-18-14351-2018, 2018.

Haag, W., Kärcher, B., Ström, J., Minikin, A., Lohmann, U., Ovarlez, J., and Stohl, A.: Freezing thresholds and cirrus cloud formation mechanisms inferred from in situ measurements of relative humidity, Atmos. Chem. Phys., 3, 1791–1806, https://doi.org/10.5194/acp-3-1791-2003, 2003.

Heymsfield, A., Bansemer, A. and Twohy, C.: Refinements to Ice Particle Mass Dimensional and Terminal Velocity Relationships for Ice Clouds. Part I: Temperature Dependence, J. Atmos. Sci., 64, 1047-1067, doi: 10.1175/JAS3890.1, 2007.

https://doi.org/10.5194/acp-2020-846
Preprint. Discussion started: 22 October 2020

Atmospheric Chemistry and Physics Discussions

Heymsfield, A. J. and Westbrook, C. D.: Advances in the Estimation of Ice Particle Fall Speeds Using Laboratory and Field Measurements, J. Atmos. Sci., 67, 2469–2482, 2010.

Holland, M. M., Bitz, C. M.: Polar amplification of climate change in coupled models. *Climate Dynamics* **21,** 221–232, https://doi.org/10.1007/s00382-003-0332-6, 2003.

Holland, M. M., Bitz, C. M., Tremblay, B.: Future abrupt reductions in the summer Arctic sea ice. Geophys. Res. Lett. 33, L23503. (doi:10.1029/2006GL028024), 2006.

Jensen, E. J., Leonhard, P., Lawson, P.: Using statistical comparisons between simulations and observations to understand physical processes controlling midlatitude cirrus ice size distributions, paper presented at the 16th International Conference on Clouds and Precipitation, Leipzig, Germany, 31 July 2012a.

Jensen, E. J., Pfister, L., and Bui, T. P.: Physical processes controlling ice concentrations in cold cirrus near the tropical tropopause, J. Geophys. Res., 117, D11205, doi:10.1029/2011JD017319, 2012b.

Koop, T., Luo, B., Tsias, A., and Peter, T.: Water activity as the determinant for homogeneous ice nucleation in aqueous solutions, Nature, 406, 611-614, 2000.

Korolev, A. V., Emery, E. F., Strapp, J. W., Cober, S. G., Isaac, G. A., Wasey, M. and Marcotte, D.: Small ice particles in tropospheric clouds: Fact or artifact? Bull. Amer. Meteorol. Soc., August, 967-973, doi:10.1175/2010BAMS3141.1, 2011.

Korolev, A., and Field, P. R.: Assessment of the performance of the inter-arrival time algorithm to identify ice shattering artifacts in cloud particle probe measurements, Atmos. Meas. Tech., 8, 761–777, doi:10.5194/amt-8-761-2015, 2015.

Krämer, M., Rolf, C., Luebke, A., Afchine, A., Spelten, N., Costa, A., Meyer, J., Zoeger, M., Smith, J., Herman, R. L., Buchholz, B., Ebert, V., Baumgardner, D., Borrmann, S., Klingebiel, M., and Avallone, L.: A microphysics guide to cirrus clouds - Part 1: Cirrus types, Atmospheric Chemistry and Physics, 16, 3463–3483, doi:10.5194/acp-16-3463-2016, 2016.

Krämer, M., Rolf, C., Spelten, N., Afchine1, A., Fahey, D., Jensen, E., Khaykin, S., Kuhn, T., Lawson, P., Lykov, A., Pan, L., Riese, M., Rollins, A., Stroh, F., Thornberry, T., Wolf, V., Woods, S., Spichtinger, P., Quaas, J., and Sourdeval, O.: A micophysics guide to cirrus – Part 2: Climatologies of clouds and humidity from observations, Atmos. Chem. Phys. Discuss., https://doi.org/10.5194/acp-2020-40, 2020.

Kristjánsson, J. E., Muri, H., and Schmidt, H.: The hydrological cycle response to cirrus cloud thinning. Geophys. Res. Lett., 42, 10 807–10 815, https://doi.org/10.1002/2015GL066795, 2015.

Kuebbeler, M., Lohmann, U., Hendricks, J. and Kärcher, B.: Dust ice nuclei effects on cirrus clouds, Atmos. Chem. Phys., 14, 3027–3046, doi:10.5194/acp-14-3027-2014, 2014.

Lawson, R. P.: Effects of ice particles shattering on the 2D-S probe, Atmos. Meas. Tech., 4, 1361–1381, doi:10.5194/amt-4-1361-2011, 2011.

Lawson, R. P., Woods, S., and Morrison, H.: The microphysics of ice and precipitation development in tropical cumulus clouds. J. Atmos. Sci., 72, 2429–2445, doi:10.1175/JAS-D-14-0274.1, 2015.

Lawson, R. P., Gurganus, C., Woods, S., and Bruintjes, R.: Aircraft observations of cumulus microphysics ranging from the tropics to midlatitudes: Implications for a “new” secondary ice process, J. Atmos. Sci., 74, 2899-2920, 2017.

Li, Y., Thompson, D. W. J., and Bony, S.: The influence of atmospheric cloud radiative effects on the large-scale atmospheric circulation. J. Climate, 28, 7263-7278, 2015.

Li, Y., and Thompson, D. W. J.: Observed signatures of the barotropic and baroclinic annular modes in cloud vertical structure and cloud radiative effects. J. Climate, 29, 4723-4740, 2016.

Li, Y., Thompson, D. W. J., and Huang, Y.: The influence of atmospheric cloud radiative effects on the large-scale stratospheric circulation. J. Climate, 30, 5621-5635, 2017.

Liu, X. H. and Penner, J. E.: Ice nucleation parameterization for global models, Meteorol. Z., 14, 499–514, doi:10.1127/0941-2948/2005/0059, 2005.

McCluskey, C. S., Hill, T. C. J., Humphries, R. S., Rauker, A. M., Moreau, S., Strutton, P. G., S. D. Chambers, S. D., Williams, A. G., McRobert, I., Ward, J., Keywood, M. D., Harnwell, J., Ponsonby, W., Loh, Z. M., Krummel, P. B., Protat, A., Kreidenweis, and DeMott, P. J.: Observations of ice nucleating particles over Southern Ocean waters. Geophysical Research Letters, 45, 11,989–11,997. https://doi.org/10.1029/2018GL079981, 2018.

Mishra, S., Mitchell, D. L., Turner, D. D., and Lawson, R. P.: Parameterization of ice fall speeds in midlatitude cirrus: results from SPartICus, J. Geophys. Res.-Atmos., 119, 3857–3876, https://doi.org/10.1002/2013jd020602, 2014.

Mitchell, D. L.: Use of mass- and area-dimensional power laws for determining precipitation particle terminal velocities, J. Atmos. Sci., 53, 1710–1723, 1996.

Mitchell, D. L.: Effective diameter in radiation transfer: general definition, applications, and limitations, J. Atmos. Sci., 59, 2330–2346, https://doi.org/10.1175/1520-0469(2002)059<2330:edirtg>2.0.co;2, 2002.

Mitchell, D. L., Zhang, R., and Pitter, R. L.: Mass-dimensional relationships for ice particles and the influence of riming on snowfall rates, J. Appl. Meteorol., 29, 153–163, 1990.

Mitchell, D. L. and Heymsfield, A. J.: Refinements in the treatment of ice particle terminal velocities, highlighting aggregates, J. Atmos. Sci., 62, 1637–1644, 2005.

Mitchell, D. L., Huggins, A., and Grubisic, V.: A new snow growth model with application to radar precipitation estimates, Atmos. Res., 82, 2–18, 2006.

Mitchell, D. L., Rasch, P., Ivanova, D., McFarquhar, G. and Nousiainen, T.: Impact of small ice crystal assumptions on ice sedimentation rates in cirrus clouds and GCM simulations, Geophys. Res. Lett., 35, L09806, doi:10.1029/2008GL033552, 2008.

Mitchell, D. L., Mishra, S., and Lawson, R. P.: Representing the ice fall speed in climate models: results from tropical composition, cloud and climate coupling (TC4) and the indirect and semidirect aerosol campaign (ISDAC), J. Geophys. Res.-Atmos., 116, D00t03, https://doi.org/10.1029/2010jd015433, 2011.

Mitchell, D. L., Garnier, A., Avery, M., and Erfani, E.: CALIPSO observations of the dependence of homo- and heterogeneous ice nucleation in cirrus clouds on latitude, season and surface condition, Atmos. Chem. Phys. Discuss., https://doi.org/10.5194/acp-2016-1062, 2016.

Mitchell, D. L., Garnier, A., Pelon, J., and Erfani, E.: CALIPSO (IIR-CALIOP) retrievals of cirrus cloud ice particle concentrations. Atmos. Chem. Phys., 18, 17325–17354, https://doi.org/10.5194/acp-18-17325-2018, 2018.

Muri, H., Kristjánsson, J. E., Storelvmo, T., & Pfeffer, M. A.: The climatic effects of modifying cirrus clouds in a climate engineering framework. J. Geophys. Res., 119, 4174–4191, https://doi.org/10.1002/2013JD021063, 2014.

Muri, H., Tjiputra, J., Otterå, O. H., Adakudlu, M., Lauvset, S. K., Grini, A., Schulz, M., Niemeier, U. and Kristjánsson, J. K.: Climate response to aerosol geoengineering: A multimethod comparison, J. Climate, 31, 6319-6340, doi: 10.1175/JCLI-D-17-0620.1, 2018.

Notz, D.: The future of ice sheets and sea ice: between reversible retreat and unstoppable loss. Proc. Natl Acad. Sci. USA 106, 20 590–20 595. (doi:10.1073/pnas.0902356106), 2009.

Penner, J. E., Zhou, C., & Liu, X.: Can cirrus cloud seeding be used for geoengineering? Geophys. Res. Lett., 42, 8775–8782, https://doi.org/10.1002/2015GL065992, 2015.

Petty, G. W.: A First Course in Atmospheric Radiation. Sundog Publishing, Madison, Wisconsin, 2006.

Shi, X., Liu, X. and Zhang, K.: Effects of pre-existing ice crystals on cirrus clouds and comparison between different ice nucleation parameterizations with the Community Atmosphere Model (CAM5), Atmos. Chem. Phys., 15, 1503–1520, 2015.

Sourdeval, O., Gryspeerdt, E., Krämer, M., Goren, T., Delanoë, J., Afchine, A., Hemmer, F., and Quaas, J.: Ice crystal number concentration estimates from lidar-radar satellite remote sensing, Part 1: Method and evaluation, Atmos. Chem. Phys., 18, 14327–14350, https://doi.org/10.5194/acp-18-14327-2018, 2018.

Spichtinger, P., and Krämer, M.: Tropical tropopause ice clouds: a dynamic approach to the mystery of low crystal numbers, Atmos. Chem. Phys., 13, 9801-9818, 2013.

Storelvmo, T., Kristjansson, J. E., Muri, H., Pfeffer, M., Barahona, D., and Nenes, A.: Cirrus cloud seeding has potential to cool climate. Geophys. Res. Lett., 40, 178–182, https://doi.org/10.1029/2012GL054201, 2013.

Storelvmo, T. and Herger, N.: Cirrus cloud susceptibility to the injection of ice nuclei in the upper troposphere, J. Geophys. Res.-Atmos., 119, 2375–2389, https://doi.org/10.1002/2013JD020816, 2014.

Storelvmo, T., Boos, W. R., and Herger, N.: Cirrus cloud seeding: a climate engineering mechanism with reduced side effects?, Phil. Trans. R. Soc. A, 372, 20140116, https://doi.org/10.1098/rsta.2014.0116, 2014.

Vergara-Temprado, J., Miltenberger, A. K., Furtado, K., Grosvenor, D. P., Shipway, B. J., Hill, A. A., Wilkinson, J. M., Field, P. R., Murray, B. J., and Carslaw, K. S.: Strong control of Southern Ocean cloud reflectivity by ice-nucleating particles, P. Natl. Acad. Sci. USA, 115, 2687–2692, 2018.

Zhao, B., Liou, K.-N., Gu, Y., Jiang, J. H., Li, Q., Fu, R., Huang, L., Liu, X., Shi, X., Su, H., and He, C.: Impact of aerosols on ice crystal size, Atmos. Chem. Phys., 18, 1065–1078, https://doi.org/10.5194/acp-18-1065-2018, 2018.

Zhao, F., Tang, C., Dai, C., Wu, X. and Wei, H.: The Global Distribution of Cirrus Clouds Reflectance Based on MODIS Level-3 Data, Atmosphere, 11, 219; doi:10.3390/atmos11020219, 2020.

https://doi.org/10.5194/acp-2020-846
Preprint. Discussion started: 22 October 2020

Atmospheric Chemistry and Physics Discussions

Table 1. WACCM6 Cases Discussed in the Text

Case Name	Description
WACCM	standard version of WACCM6 without modifications
CALCAL	WACCM6 with modified MG2 scheme based on CALIPSO D_e retrievals
HET	WACCM6 with modified MG2 scheme based on CALIPSO D_e retrievals from tropics only

Table 2. Global annual mean radiative flux comparisons (W m^{-2}) between our standard WACCM6 simulation, published WACCM6 results (Gettelman et al., 2019) and satellite observations from CERES EBAF 2.4 (Loeb et al., 2009). FLNT and FSNT are top-of-model net longwave and shortwave fluxes for all sky conditions, respectively, while LWCRE and SWCRE are top-of-model net longwave and shortwave cloud radiative effects (FLNT & FSNT minus corresponding clear sky net fluxes), respectively.

Variable	WACCM6 (40-year run)	Published WACCM6 results	Observations
FLNT	237.7	237.4	239.7
FSNT	240.9	241.0	240.5
LWCRE	24.4	24.6	26.1
SWCRE	-48.0	-48.4	-47.1

Table 3. Differences in cloud radiative effect (CRE) for the simulations of this study for the global annual mean and for annual means outside the tropics, where NH = Northern Hemisphere (30N – 90N) and SH = Southern Hemisphere (30S – 90S). Units are W m^{-2}.

	WACCM – CALCAL	WACCM – HET	HET – CALCAL
Global	-0.132	1.03	-1.16
NH	-1.63	0.744	-2.37
SH	-2.59	-0.0437	-2.55

Table 4. Differences in total net forcing at TOM (top of model) for the simulations of this study for the global annual mean and for annual means outside the tropics, where NH = Northern Hemisphere (30N – 90N) and SH = Southern Hemisphere (30S – 90S). Units are W m^{-2}.

	WACCM – CALCAL	WACCM – HET	HET – CALCAL
Global	0.188	1.12	-0.929
NH	-1.12	0.654	-1.77
SH	-1.94	0.0887	-2.03

https://doi.org/10.5194/acp-2020-846
Preprint. Discussion started: 22 October 2020

Atmospheric Chemistry and Physics Discussions

Table 5. Differences in total net forcing at TOM (top of model) for means excluding summer in W m^{-2}, where NH = Northern Hemisphere (30N – 90N) and SH = Southern Hemisphere (30S – 90S). Excluding summer means that JJA is omitted for NH and DJF is omitted for the SH.

	WACCM – CALCAL	WACCM – HET	HET – CALCAL
NH	-1.56	0.864	-2.43
SH	-2.11	0.322	-2.43

5

https://doi.org/10.5194/acp-2020-846
Preprint. Discussion started: 22 October 2020

Atmospheric Chemistry and Physics Discussions

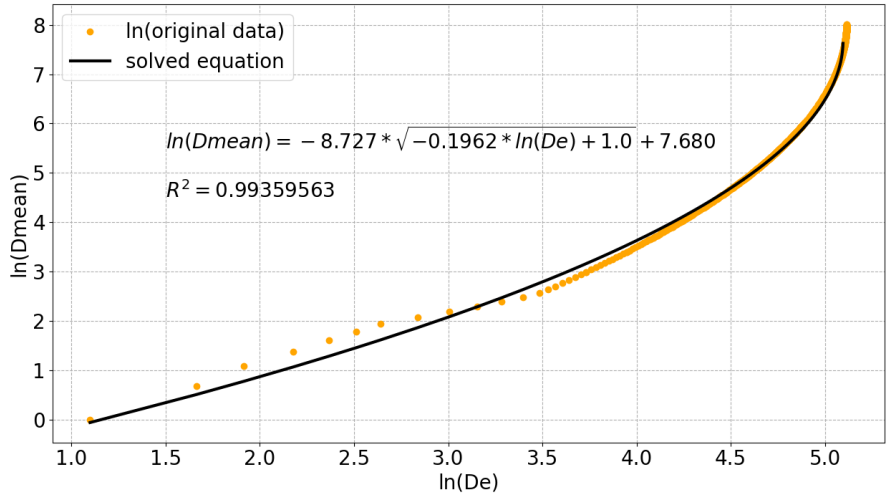

Figure 1. Relationship between D_{mean} and D_e (in μm) as predicted by Eq. 3 and the size (D) dependent m-D and A-D coefficients (α, β, γ and δ) as described in EM2016. The series of orange points were generated by the iterative solution, and the dark curve was generated by the curve-fit equation shown.

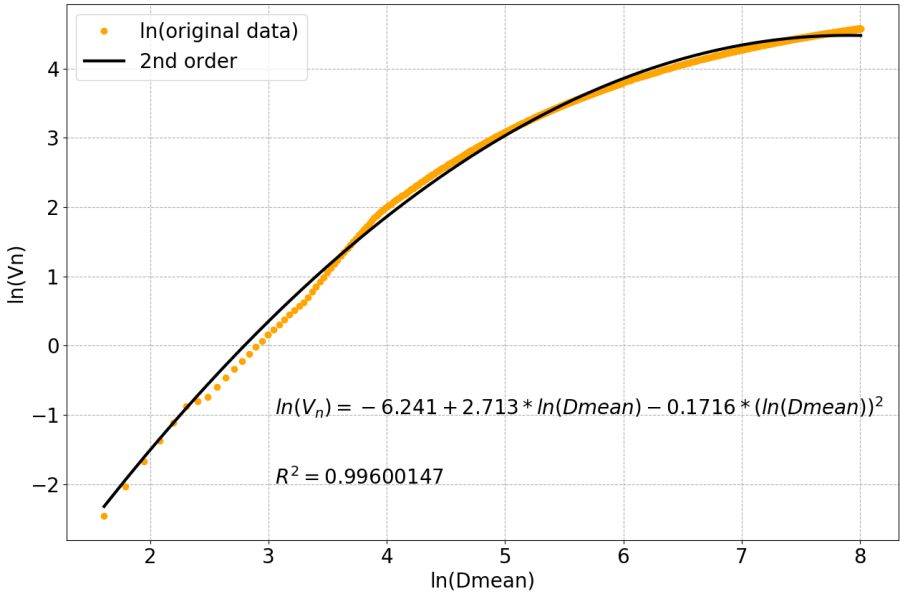

Figure 2. Comparison between generated D_{mean}-V_N values (in μm and cm s^{-1}) based on the above methodology, and the corresponding curve-fit for use in the MG2 scheme.

https://doi.org/10.5194/acp-2020-846
Preprint. Discussion started: 22 October 2020

Atmospheric Chemistry and Physics Discussions

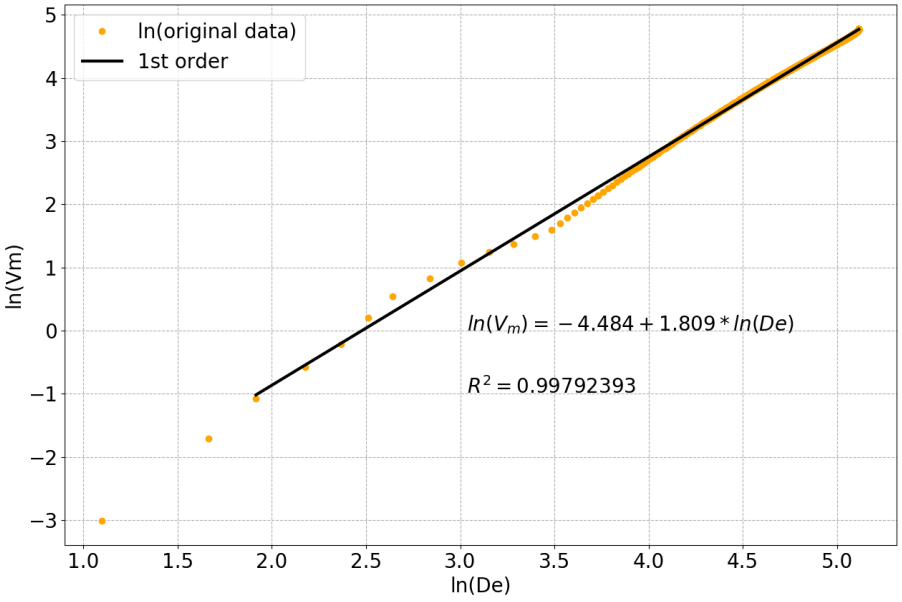

Figure 3. Comparison between generated D_e-V_m values (in µm and cm s^{-1}) based on the above methodology, and the corresponding linear-fit for use in the MG2 scheme.

https://doi.org/10.5194/acp-2020-846
Preprint. Discussion started: 22 October 2020

Atmospheric Chemistry and Physics Discussions

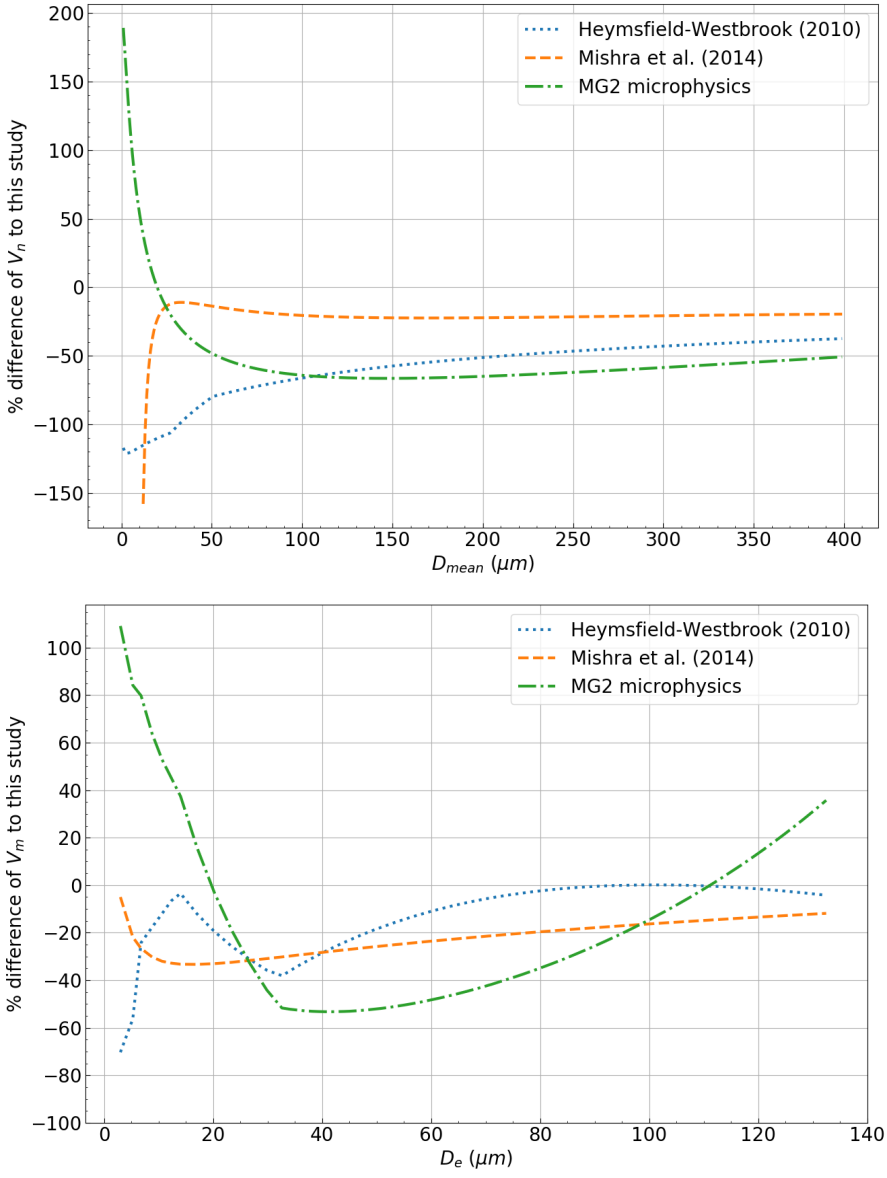

Figure 4. Comparisons of three ice fall speed schemes (including the MG2 scheme) against the scheme developed for this study. Both number- and mass-weighted fall speeds, V_N and V_m (top and lower panels, respectively), are calculated in each scheme. The closer to the zero line, the closer the agreement is.

https://doi.org/10.5194/acp-2020-846
Preprint. Discussion started: 22 October 2020

Atmospheric Chemistry and Physics Discussions

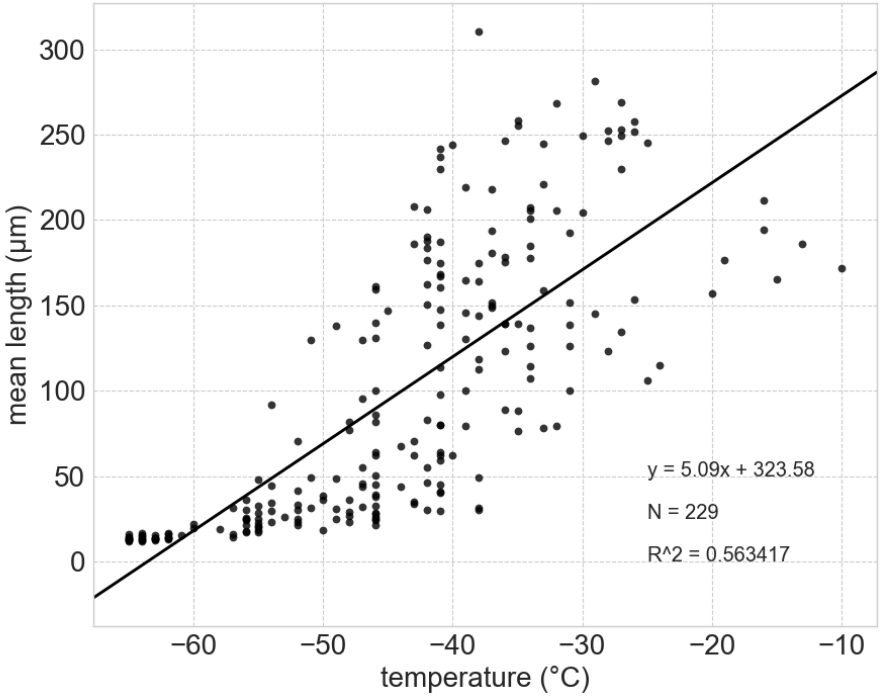

Figure 5. PSD mean maximum dimension (D_{mean}) related to sampling temperature, based on SPARTICUS data for synoptic (non-anvil) cirrus clouds. The regression line estimates D_{mean} within a factor of 3, based on the spread for any given temperature. This should be sufficiently adequate for estimating the constants used in the mass and area power laws. Regarding the range of D_{mean}, $D_{mean}(-60°C) \approx 18$ µm and $D_{mean}(0°C) \approx 324$ µm. This dataset is based on unmodified 2DS data (i.e. the smallest 2DS size bin is included). Evidence of homogeneous ice nucleation is apparent for T < -40°C.

https://doi.org/10.5194/acp-2020-846
Preprint. Discussion started: 22 October 2020

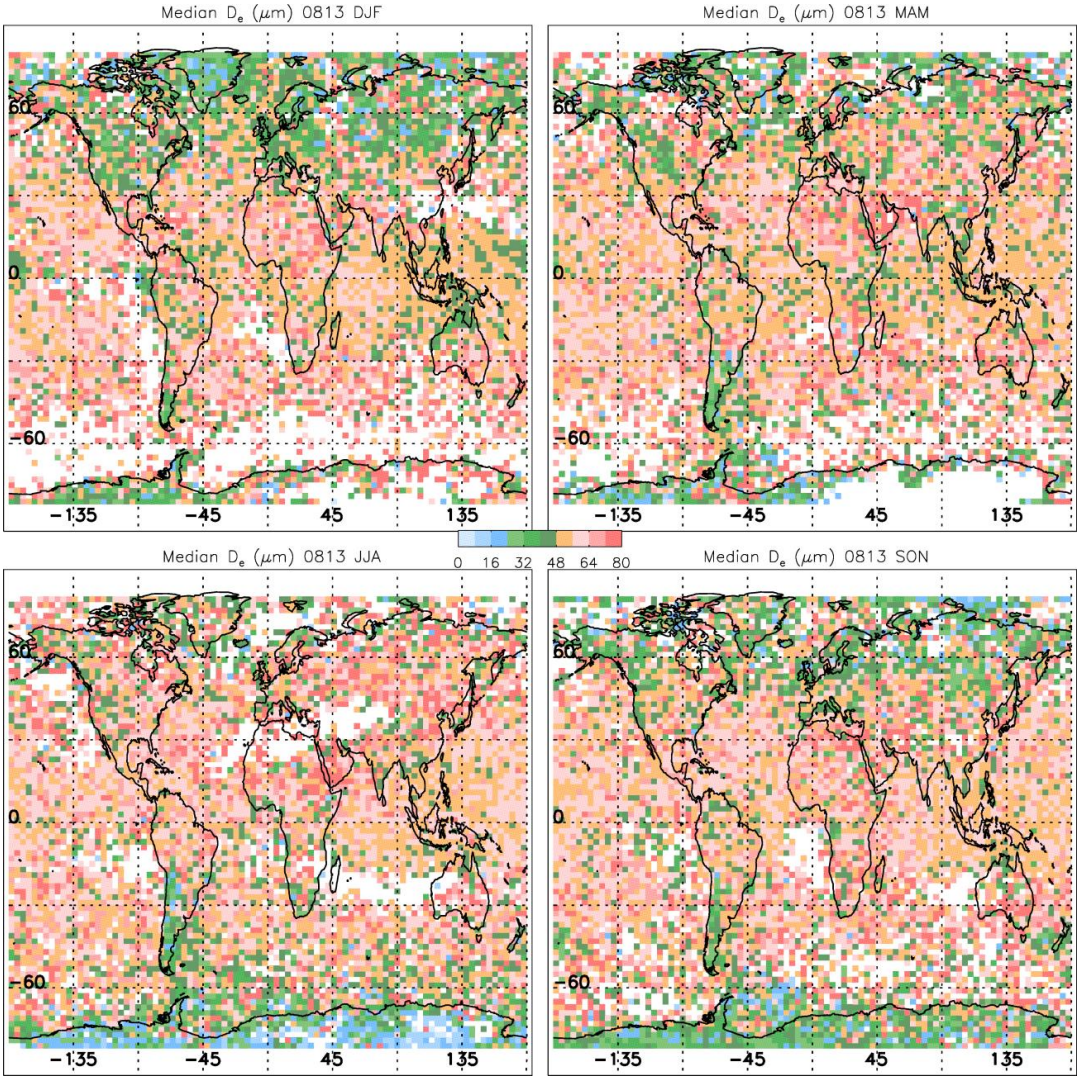

Figure 6. The seasonal dependence of median D_e (color legend at center is in μm) for temperature $T \leq 235$ K for the years 2008 and 2013, based on the first formulation (SPARTICUS in situ data with $N(D)_1$ included) of the CALIPSO retrieval.

https://doi.org/10.5194/acp-2020-846
Preprint. Discussion started: 22 October 2020

Atmospheric Chemistry and Physics Discussions

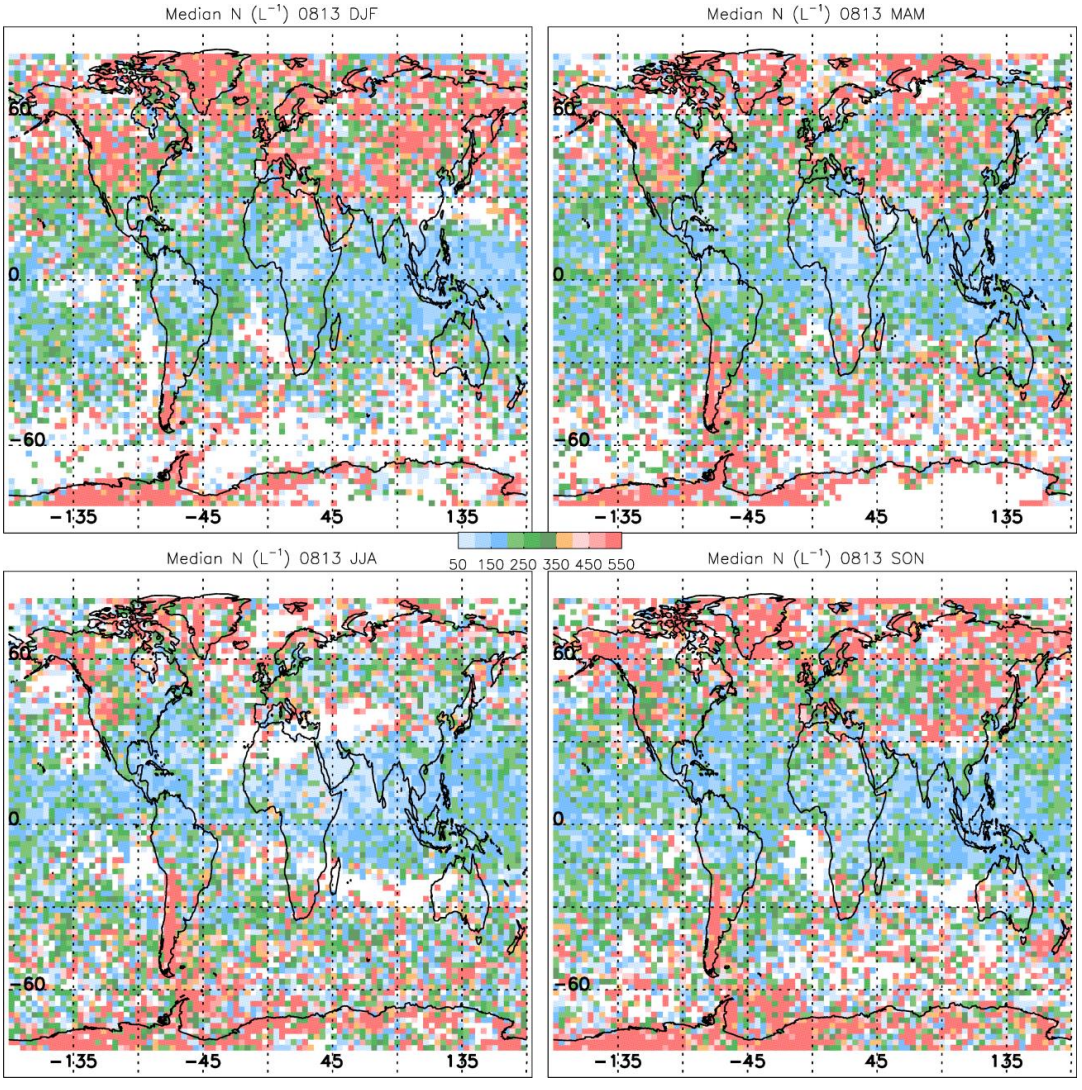

Figure 7. The seasonal dependence of median N (color legend at center is in L^{-1}) for $T \leq 235$ K for the years 2008 and 2013, based on the first formulation (SPARTICUS in situ data with $N(D)_1$ included) of the CALIPSO retrieval.

5

https://doi.org/10.5194/acp-2020-846
Preprint. Discussion started: 22 October 2020

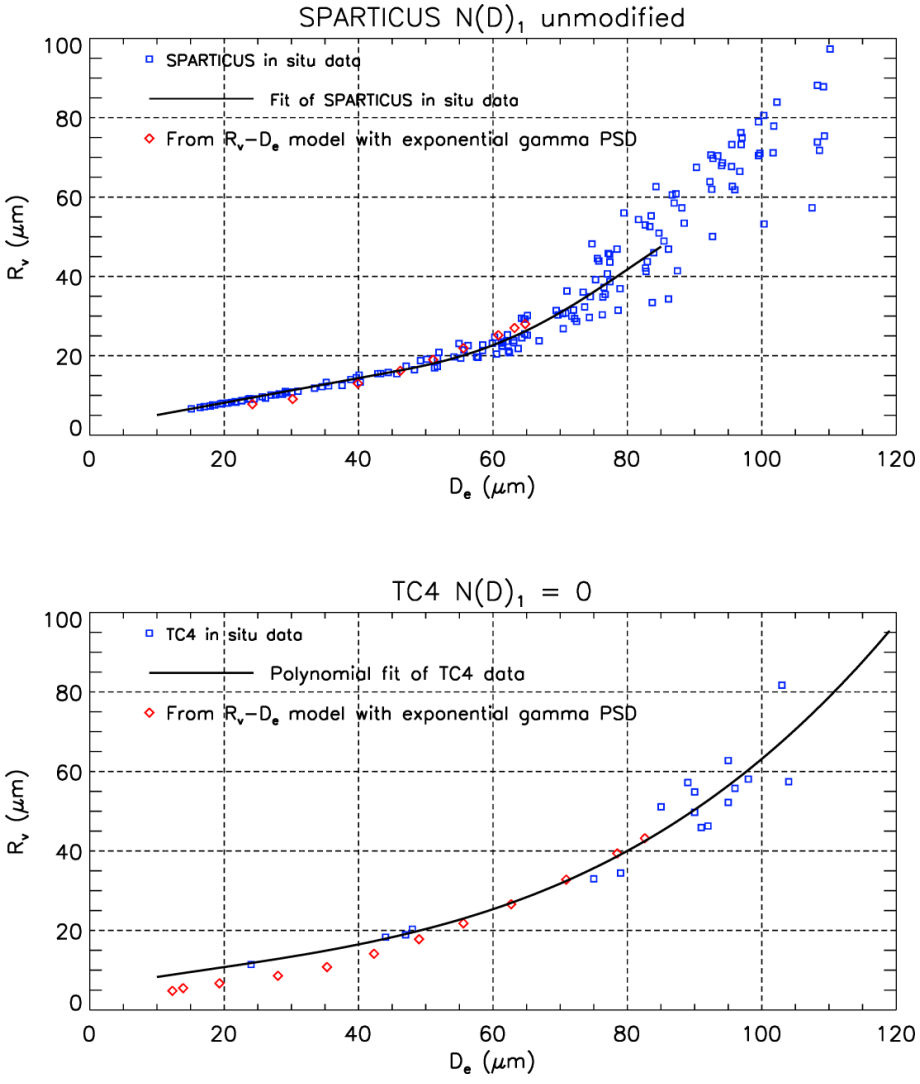

Figure 8. In situ measurements of N, A_{PSD} and IWC were calculated from 2D-S probe PSD measurements (or estimates regarding IWC) taken during the SPARTICUS and TC4 field campaigns. These were used in Eqns. (12) and (28) to calculate D_e and R_v for each PSD, shown by the blue squares. The red diamonds were determined theoretically for exponential PSD (see text for details). The curve fits (see Appendix B) were used to convert retrieved D_e to R_v, where the TC4 fit is applied to tropical D_e and the SPARTICUS fit to midlatitude D_e.

https://doi.org/10.5194/acp-2020-846
Preprint. Discussion started: 22 October 2020

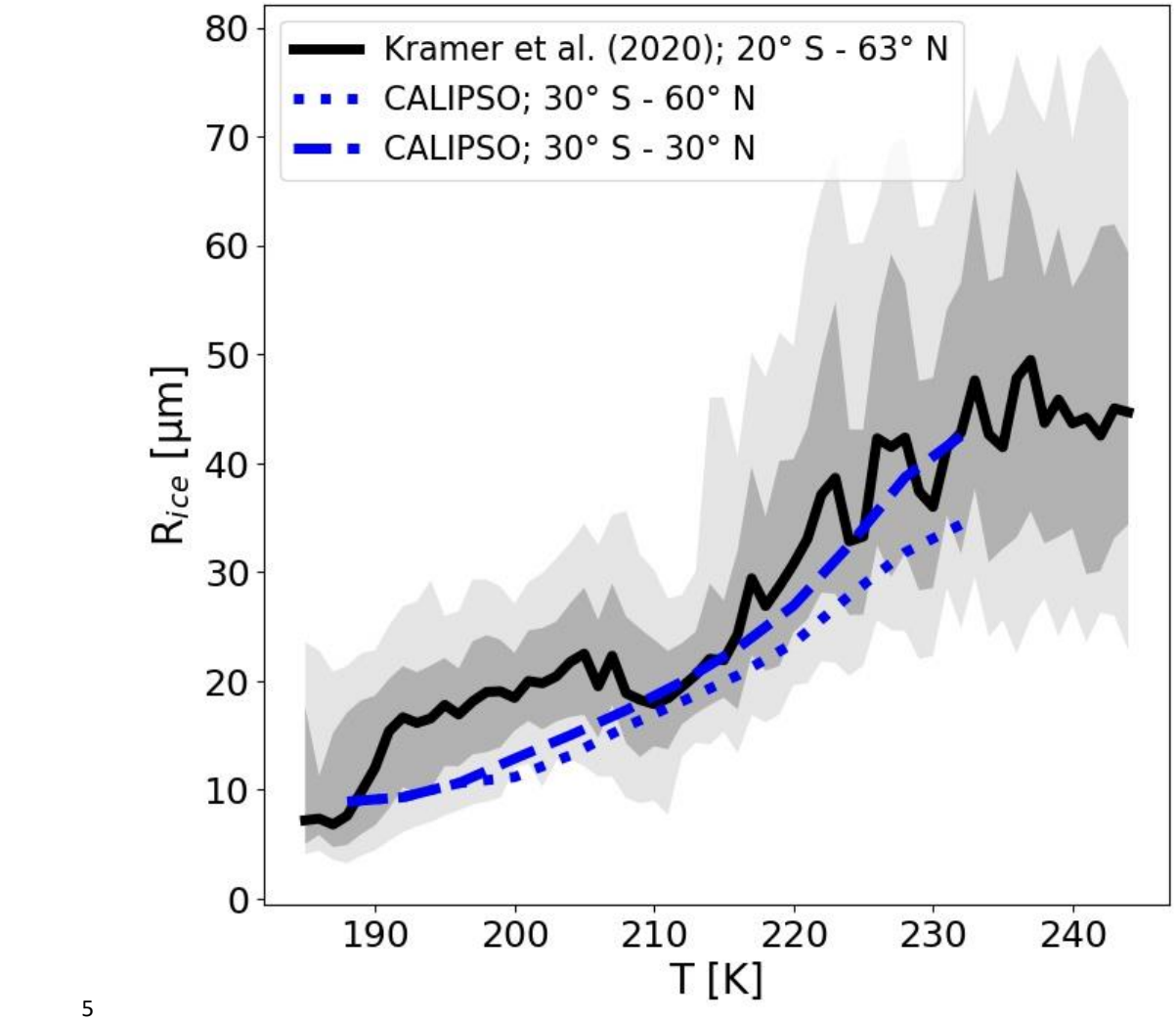

Figure 9. Comparison of the temperature-dependence of retrieval derived R_v (i.e. R_{ice}; blue curves) with median R_v from the in situ climatology of Krämer et al. (2020) shown by the black curve. The grey envelope gives the 25 and 75 percentiles while the light grey gives the 10 and 90 percentiles for the in situ R_v. The dashed blue curve is for the tropics only (± 30 °latitude) while the dotted blue curve is averaged over the midlatitudes and tropics.

https://doi.org/10.5194/acp-2020-846
Preprint. Discussion started: 22 October 2020

Atmospheric Chemistry and Physics Discussions

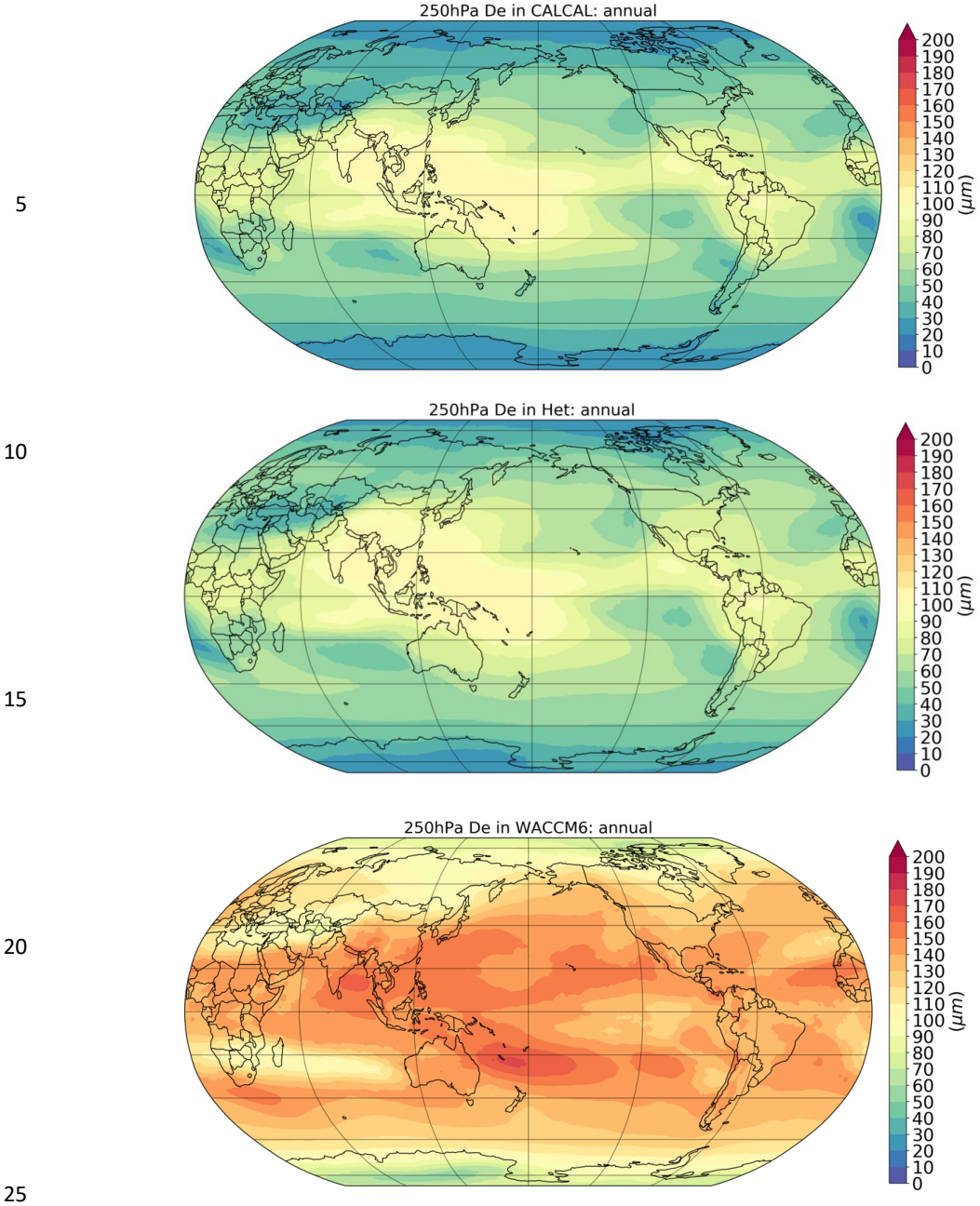

Figure 10. From top-to-bottom, annual mean CALCAL, HET, and WACCM6 simulation results for in-cloud D_e at 250 hPa in microns.

https://doi.org/10.5194/acp-2020-846
Preprint. Discussion started: 22 October 2020

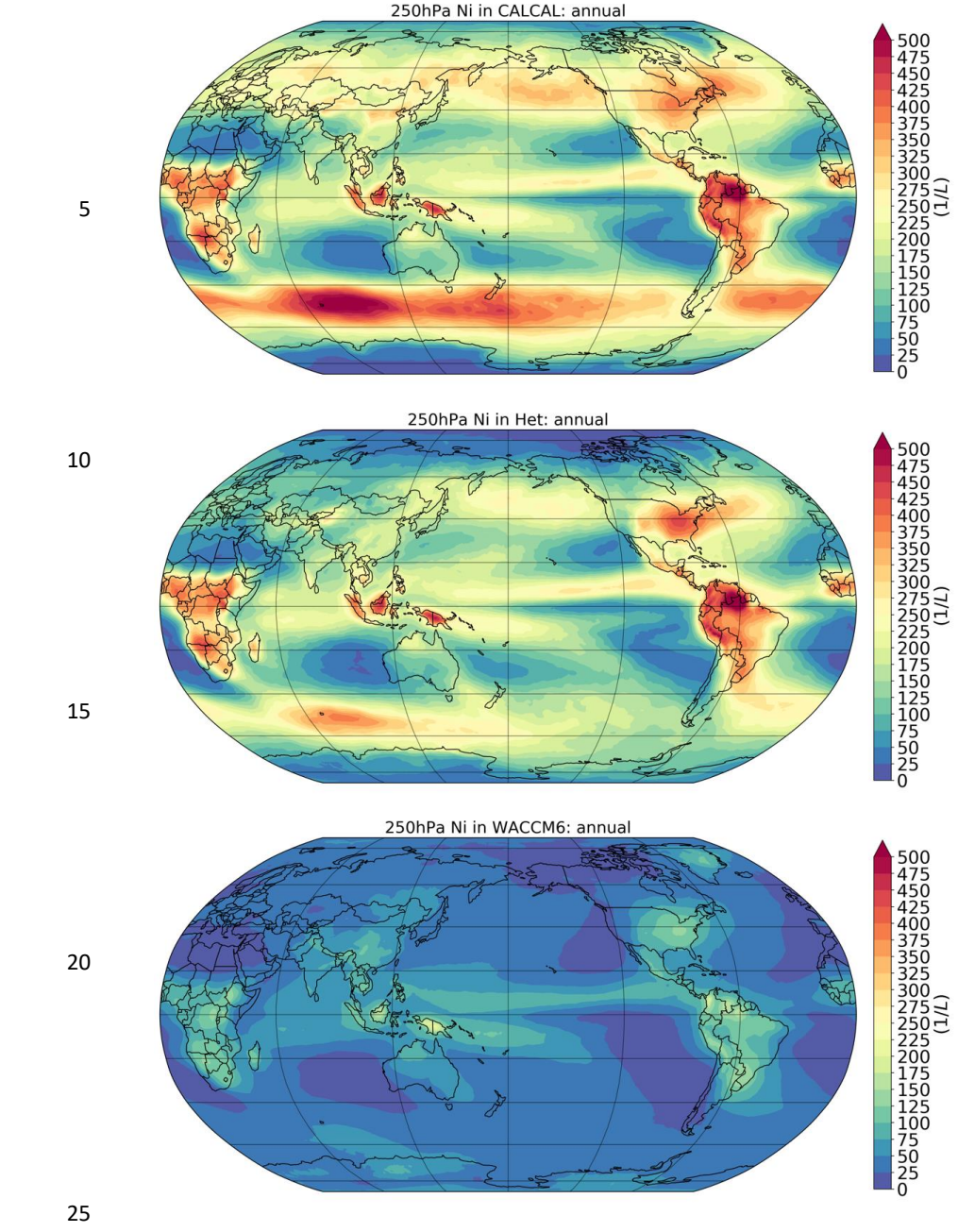

Figure 11. From top-to-bottom, annual mean CALCAL, HET and WACCM6 simulation results for in-cloud N at 250 hPa in L^{-1}.

https://doi.org/10.5194/acp-2020-846
Preprint. Discussion started: 22 October 2020

Atmospheric Chemistry and Physics Discussions

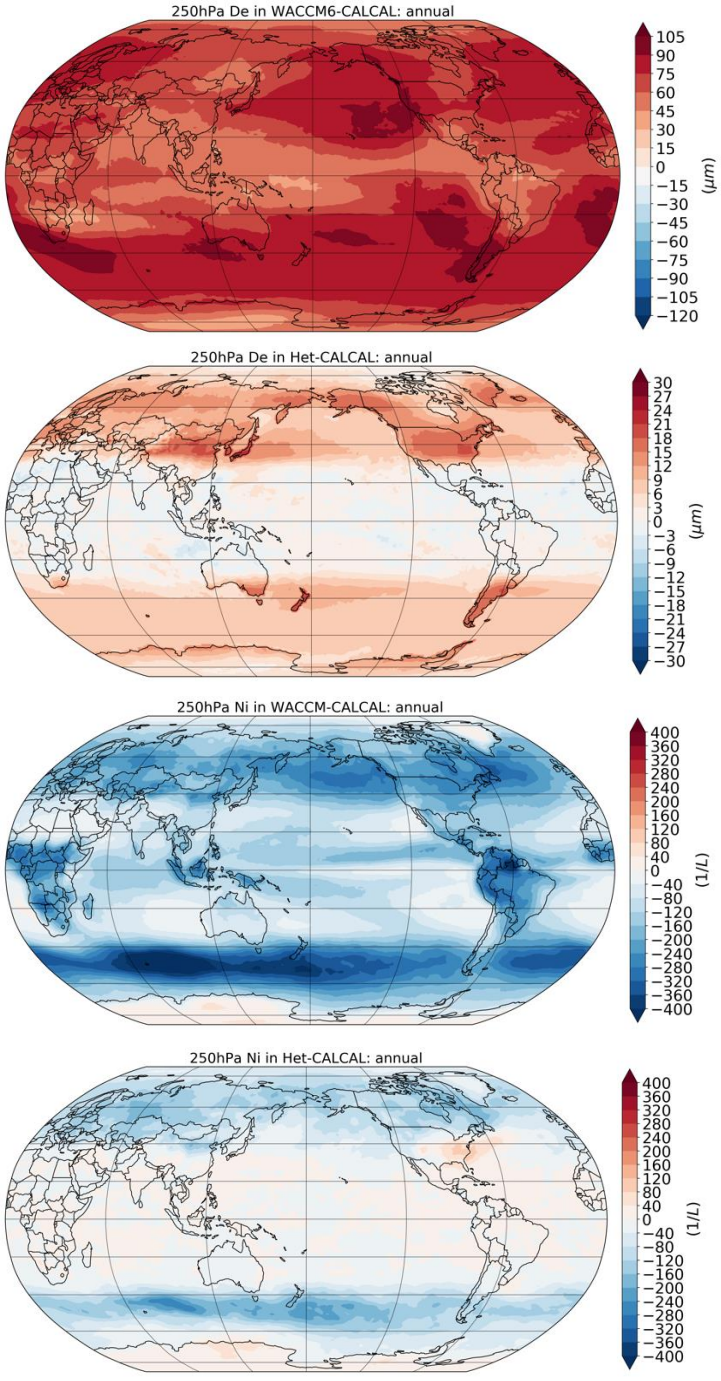

Figure 12. From top-to-bottom, WACCM6 – CALCAL, HET – CALCAL differences for D_e, and WACCM6 – CALCAL, HET – CALCAL differences for N, all at 250 hPa, based on the annual means in Figs. 10 and 11.

https://doi.org/10.5194/acp-2020-846
Preprint. Discussion started: 22 October 2020

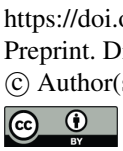

Atmospheric Chemistry and Physics Discussions

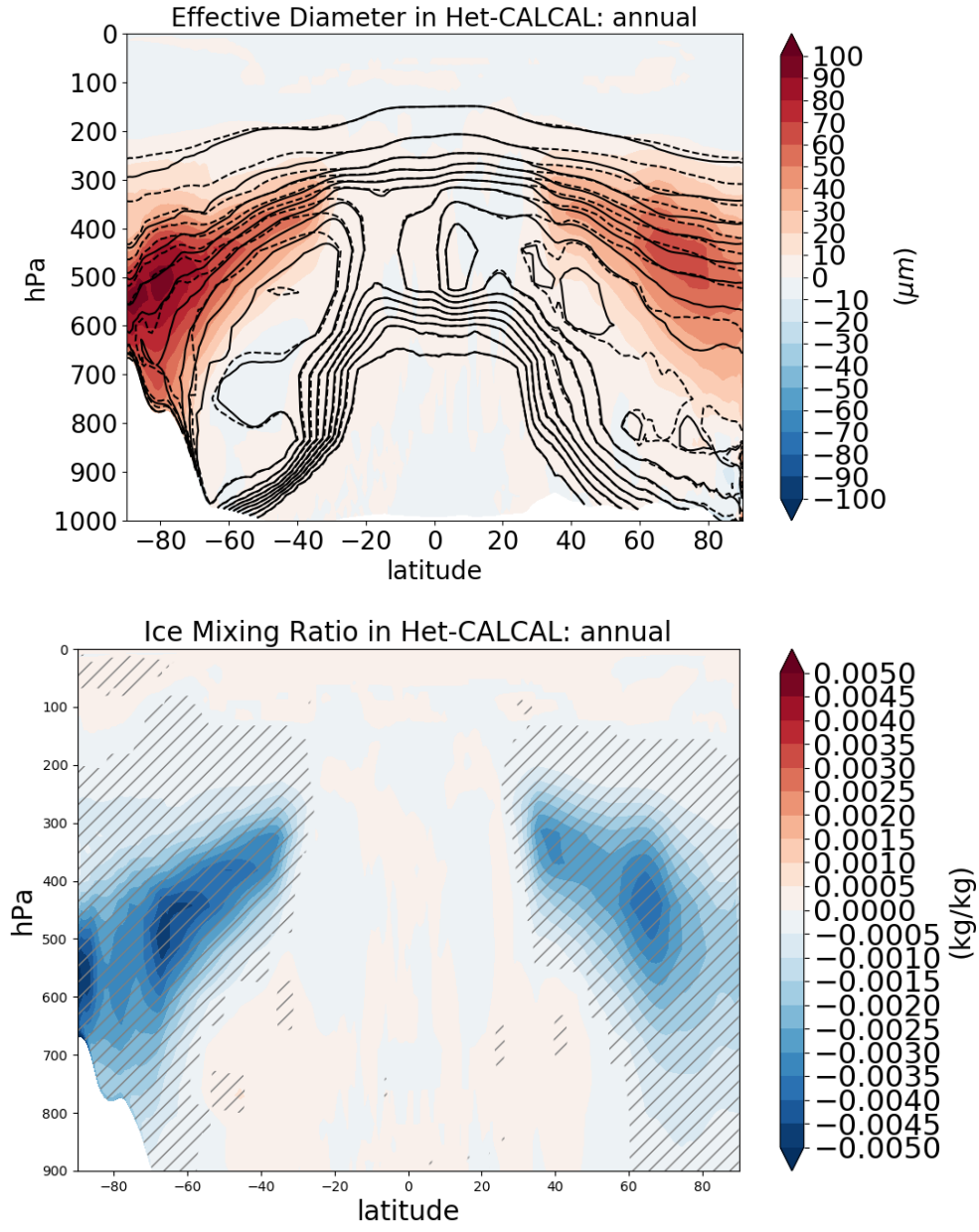

Figure 13. Upper: HET – CALCAL differences in zonal annual mean effective diameter (D_e). Solid contours are for CALCAL D_e while dashed contours are for HET D_e, each having 30 μm increments and ranging from 0 to 300 μm. The color contours represent HET – CALCAL D_e differences. Lower: Zonal mean ice water content changes are shown for different periods. The hatched areas were significantly different between HET and CALCAL with 95% confidence.

https://doi.org/10.5194/acp-2020-846
Preprint. Discussion started: 22 October 2020

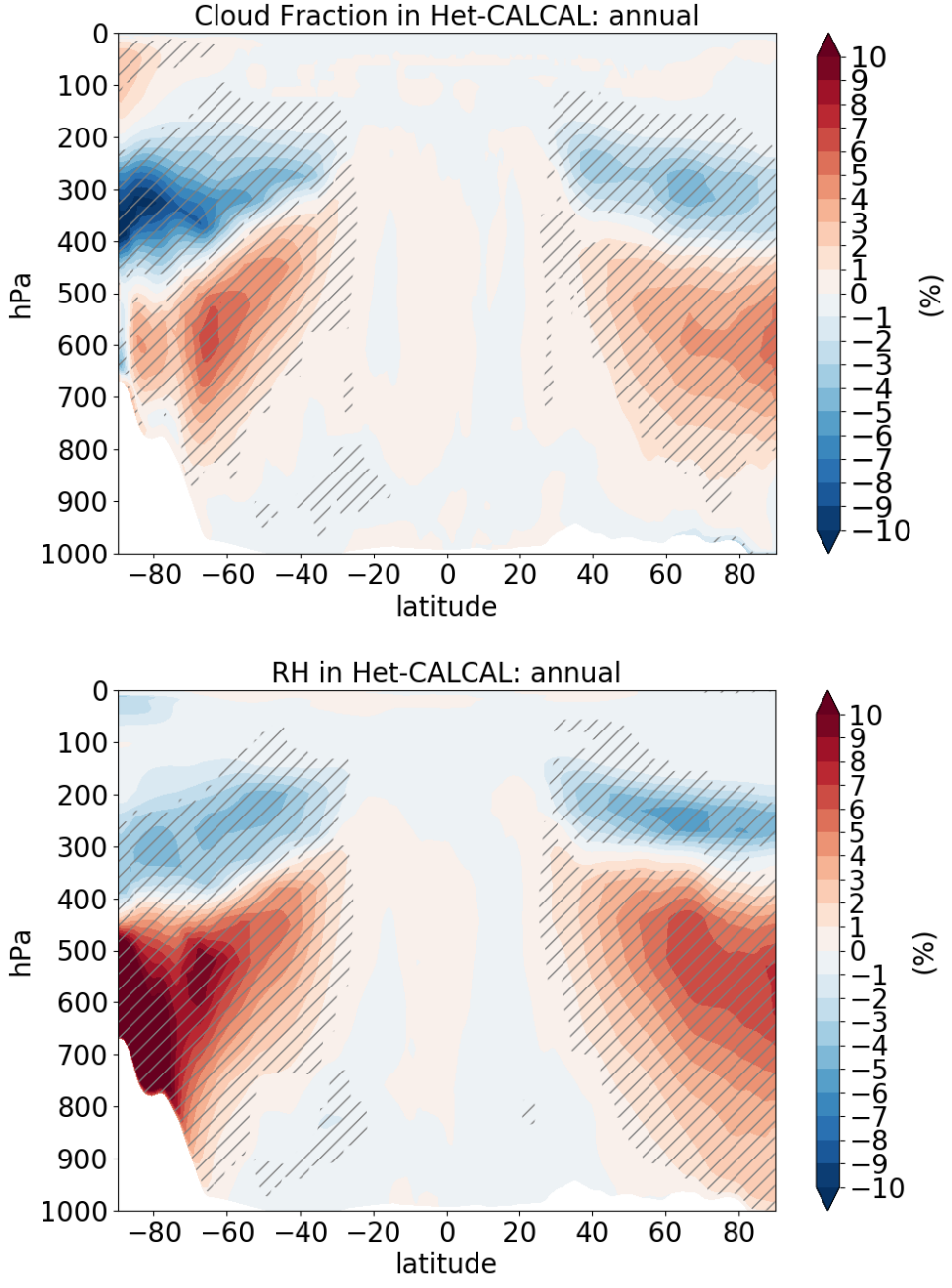

Figure 14. Upper: HET zonal mean changes (in percent) in cloud fraction relative to CALCAL. Lower: HET zonal mean relative humidity changes (in percent) relative to CALCAL. The hatched areas indicate 95% confidence that the differences are significant.

https://doi.org/10.5194/acp-2020-846
Preprint. Discussion started: 22 October 2020

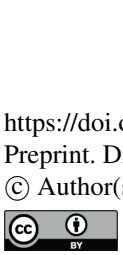

Atmospheric Chemistry and Physics Discussions

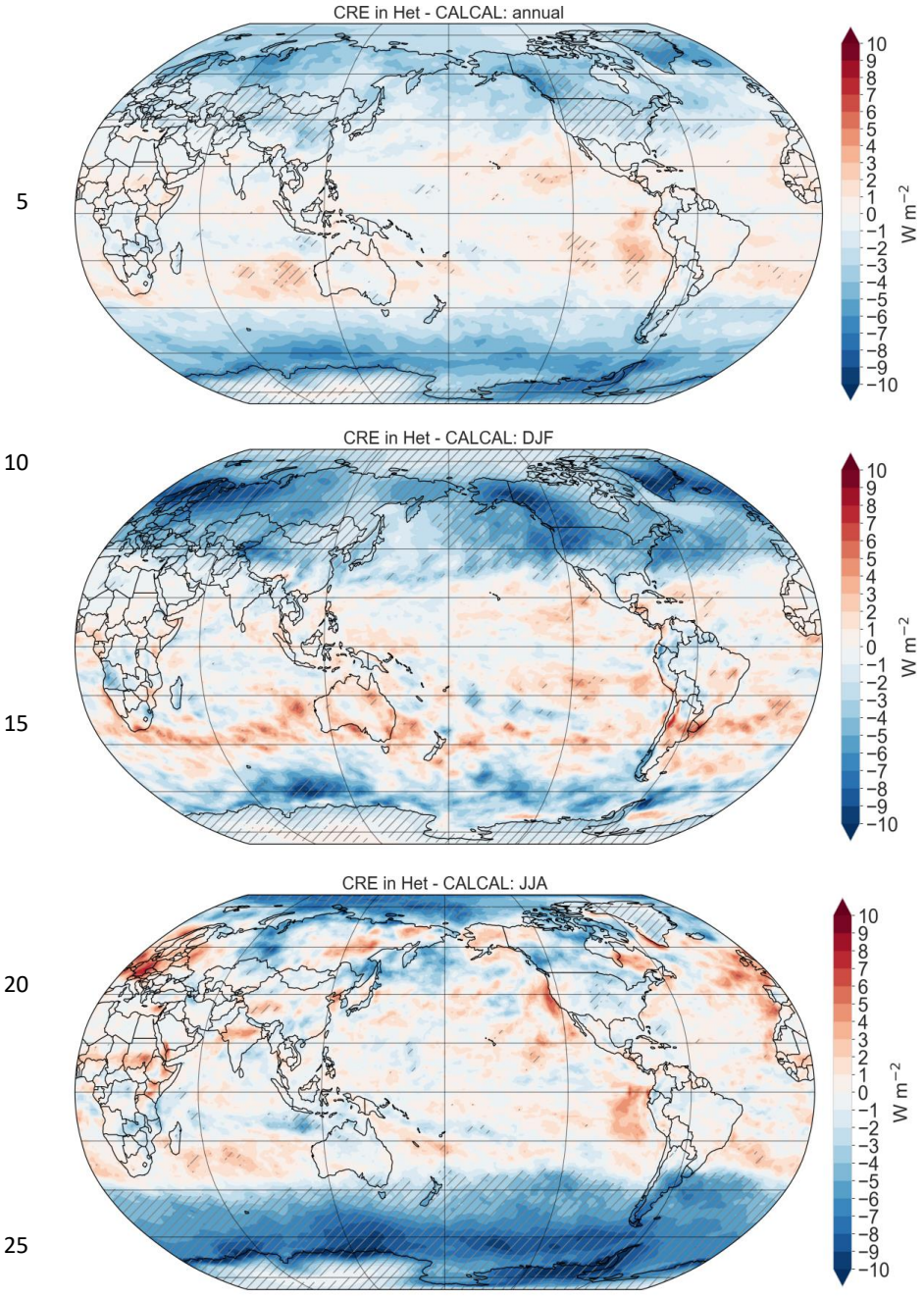

Figure 15. Annual mean and seasonal mean (DJF and JJA) HET – CALCAL differences in the cloud radiative effect (SWCF + LWCF) or CRE. Hatched areas are significant at the 95% confidence level.

https://doi.org/10.5194/acp-2020-846
Preprint. Discussion started: 22 October 2020

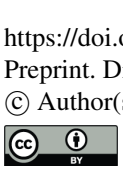

Atmospheric Chemistry and Physics Discussions

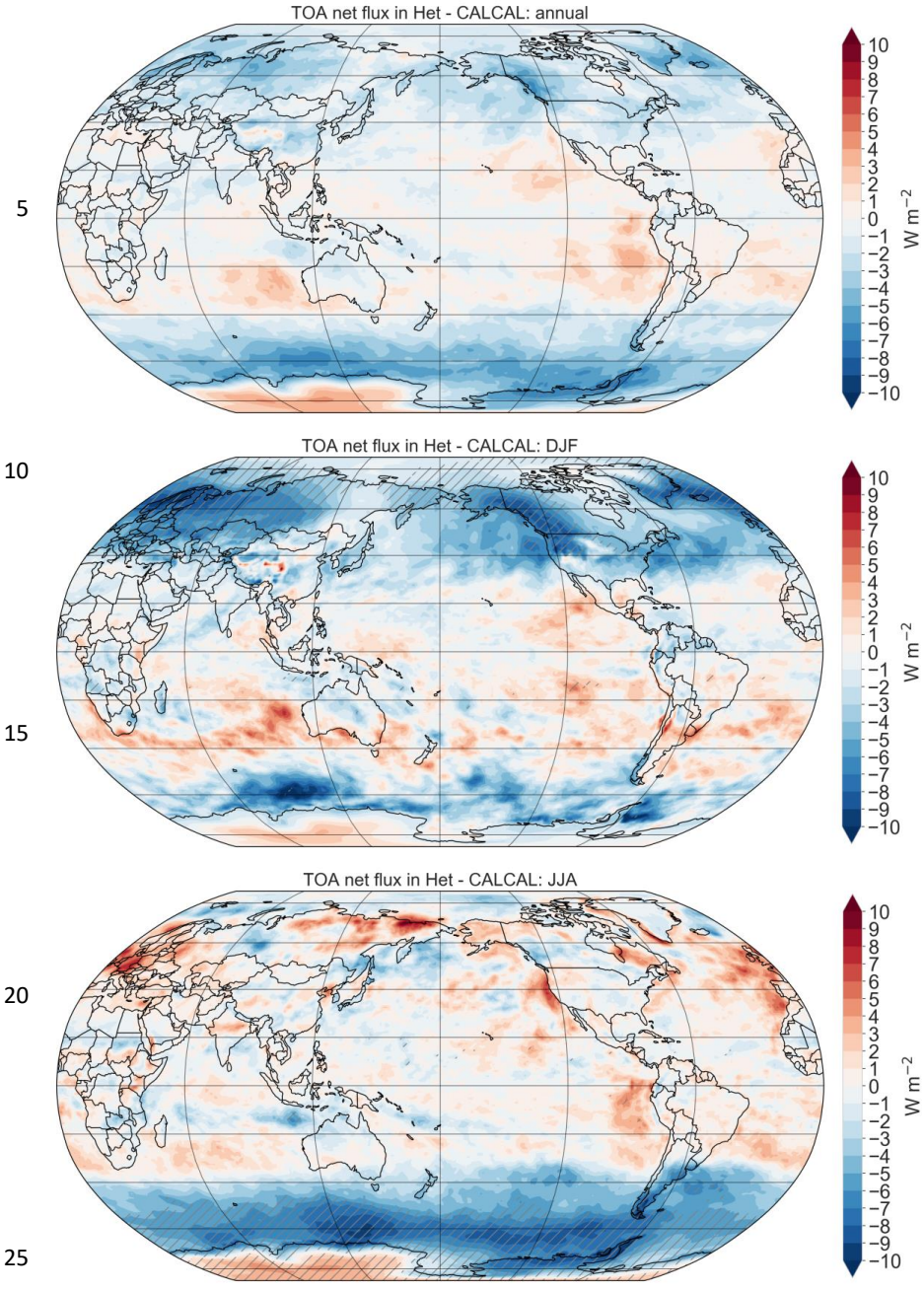

Figure 16. Top-of-model annual mean and seasonal mean (DJF and JJA) HET – CALCAL difference for all-sky net flux. Hatched areas are significant at the 95% confidence level.

https://doi.org/10.5194/acp-2020-846
Preprint. Discussion started: 22 October 2020

Atmospheric Chemistry and Physics Discussions

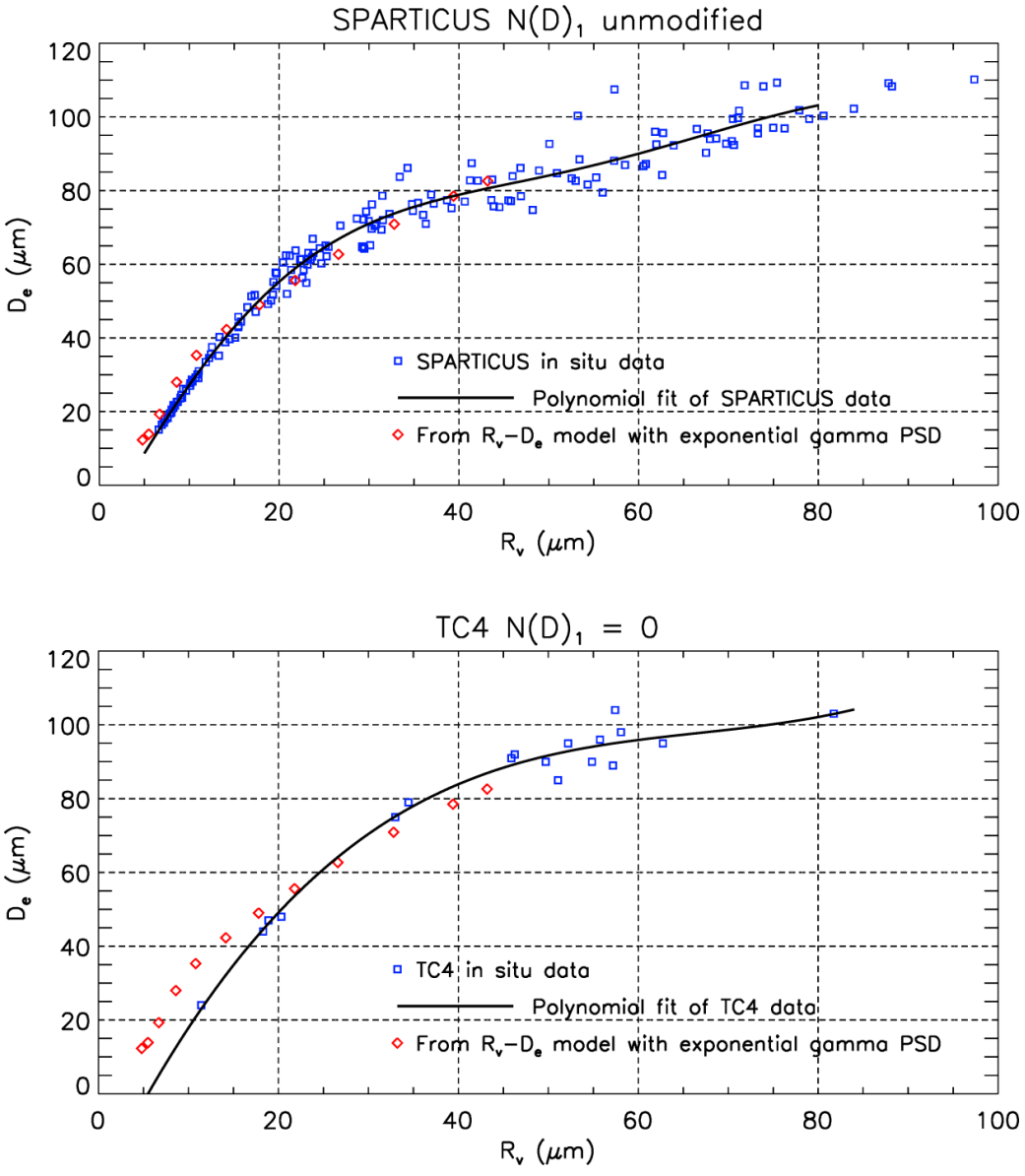

Figure B1. Similar to Fig. 8 but with reversed axes. In situ measurements of N, A_{PSD} and IWC were calculated from 2D-S probe PSD measurements (or estimates regarding IWC) taken during the SPARTICUS and TC4 field campaigns. These were used in Eqns. (12) and (28) to calculate D_e and R_v for each PSD, shown by the blue squares. The red diamonds were determined theoretically for exponential PSD (see text for details). The corresponding curve fits estimate D_e from in situ R_v (or an estimate of retrieved R_v from in situ R_v), and then estimate N from this D_e and the in situ climatology IWC.

https://doi.org/10.5194/acp-2020-846
Preprint. Discussion started: 22 October 2020

Atmospheric Chemistry and Physics Discussions

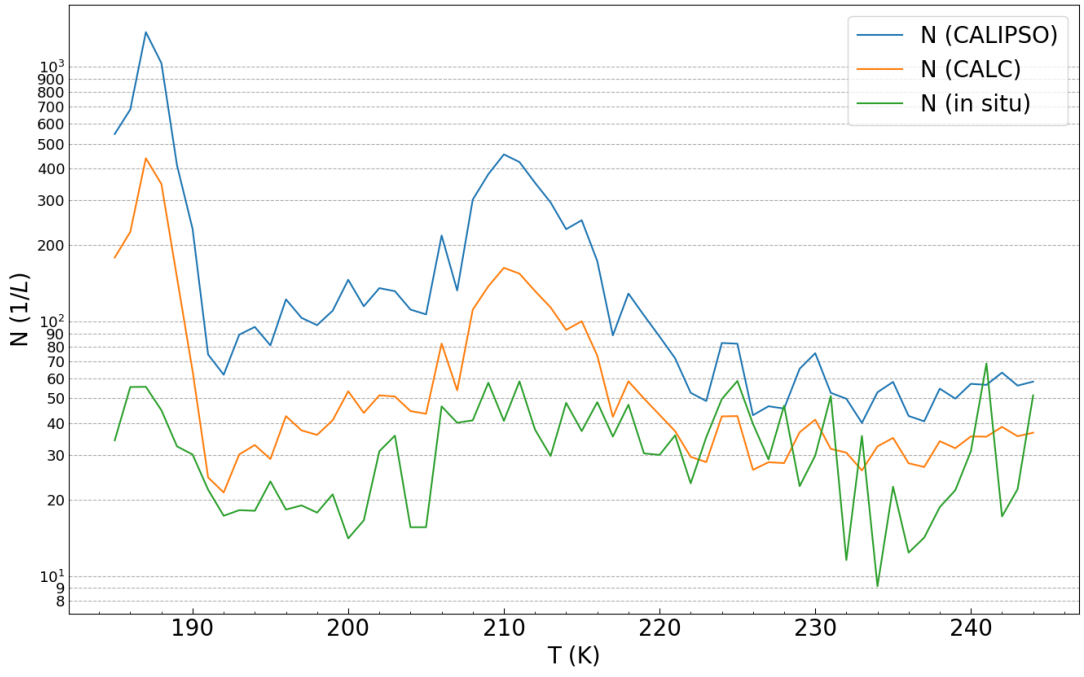

Figure B2. Results of the study comparing N calculated from in situ R_v and IWC (orange) with in situ N (green). Also shown is N calculated from R_v representing CALIPSO retrievals averaged over the tropics and midlatitudes along with the in situ IWC (blue).